

Mechanical characterization of vascular tissue using ultrasound

Inverse Method & Validation in Phantoms

Master thesis by:

Joerik de Ruijter

Supervisor:

dr. ir. R. G. P. Lopata

Committee members:

dr. ir. R. G. P. Lopata

prof. dr. ir. F. N. van de Vosse

ir. W. Huberts (MUMC+)

prof. dr. K. Ito (OPB)

Eindhoven, August 2016

Contents

Contents	3
1 Abstract	5
2 Introduction	6
2.1 General introduction	6
2.2 Goal of this study	8
3 Materials and Methods	9
3.1 The inverse approach	9
3.2 Backward displacement method	11
3.3 Optimization algorithm	12
3.3.1 Golden section search	13
3.3.2 Downhill simplex method	13
3.4 Finite element analysis	15
3.5 In Silico Testing	16
3.5.1 Test Case: Optimization Algorithm	16
3.5.2 Test Case: Influence of noise	16
3.6 PVA Phantoms	17
3.6.1 PVA preparation	17
3.6.2 Phantom preparation	17
3.7 Inflation experiment	18
3.8 Displacement tracking	19
3.9 3-D FE meshing using 2-D US-data	21
3.10 Summary framework	22
3.11 Uni-axial tensile test	23
3.11.1 Equations uni-axial tensile test	23
3.11.2 Equations inflation experiment	24
3.12 Inflation test vs uni-axial tensile test	25
4 Results	26
4.1 In Silico testing	26
4.2 Phantom construction	29
4.3 Displacement tracking	29
4.4 Estimation stress-free geometry	29
4.5 Material properties: Inverse Approach	30
4.5.1 Single layer phantoms	30
4.5.2 Double layer phantoms	31
4.6 Material properties: Uni-axial Tensile Test	38
4.7 Tensile test versus inverse approach	39

5	Discussion	40
5.1	Phantom construction and inflation experiment	40
5.2	Geometry construction	41
5.3	Inverse approach: Method	41
5.4	Inverse approach: Results	43
5.5	Uni-axial Tensile test	43
5.6	Tensile tests versus inverse approach	43
5.7	Future work	44
5.8	Conclusion	45
6	Appendix	46
	Bibliography	49

Chapter 1

Abstract

Rupture of carotid plaques accounts for 15 to 20% of ischemic strokes. To prevent a stroke patients undergo surgery, i.e. a carotid endarterectomy (CAE). However, only one out of six patients benefits from this intervention, so there is a significant overtreatment of patients. To develop better treatment criteria to improve patient diagnosis and clinical decision making, patient specific information of the plaque's composition and mechanical properties is needed. In this study, a method was developed to estimate global material properties of a large part of the vascular wall using ultrasound imaging (US). Here, we will match a finite element model (FEM) with the displacement field measured by US, by updating the material properties of the FEM. This inverse method was tested on artificial polyvinyl alcohol (PVA) phantoms, with increasing complexity, both in geometry and the number of constituents. The method was validated with uni-axial tensile testing. The estimated material properties showed good agreement with the uni-axial tensile tests.

Chapter 2

Introduction

2.1 General introduction

Cardiovascular disease (CVD) is the main cause of death worldwide [27]. Approximately 34% of CVD results in a cerebrovascular disease, such as stroke. Stroke is an important cause of cardiovascular death. A stroke is the loss of brain function because of a disruption of the brain's blood supply, mainly caused by blood clot formation elsewhere (ischemic stroke) or intracranial bleeding. Rupture of carotid plaques accounts for 15 to 20% of ischemic strokes [6]. Due to atherosclerosis a plaque can form in the carotid artery wall, usually around the bifurcation where the common carotid artery divides into the internal and external carotid artery (Figure 2.1). The plaque can consist of lipids, calcifications and fibrous connective tissue. Rupture of this plaque can result in the formation of a blood clot, which can end up in a cerebral artery, blocking the blood flow towards the brain. To prevent a stroke patients can undergo surgery, i.e., a carotid endarterectomy (CEA), where the stenosis inside the artery and intima are removed. The mortality risk due to CEA is 3 to 6%. Moreover, only one out of six patients benefits from this intervention, so there is a significant overtreatment of patients [33]. The operation is performed in patients with a 70-99% stenosis. The degree of stenosis, i.e. the percentage of occlusion, is measured using duplex ultrasound examination. However, the degree of stenosis does not determine the vulnerability of the plaque, since vulnerability depends on the plaque's morphology, mechanical properties, and the force acting on the plaque. Besides, plaques where the stenosis is less than 70% can be vulnerable, so this group of patients is not recruited for elective treatment based

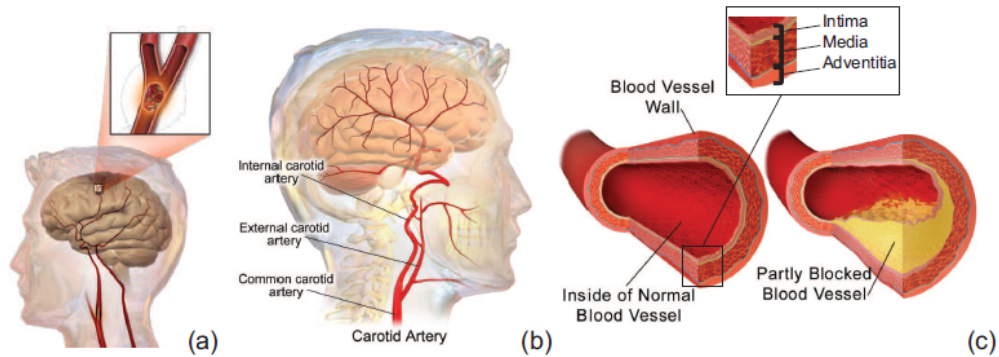


Figure 2.1: Stroke caused by debris from a ruptured plaque (a). The anatomy of the carotid artery (b). A healthy vessel and a blood vessel without and with a lipid area in the intima of the vessel wall (c). From Blausen.com

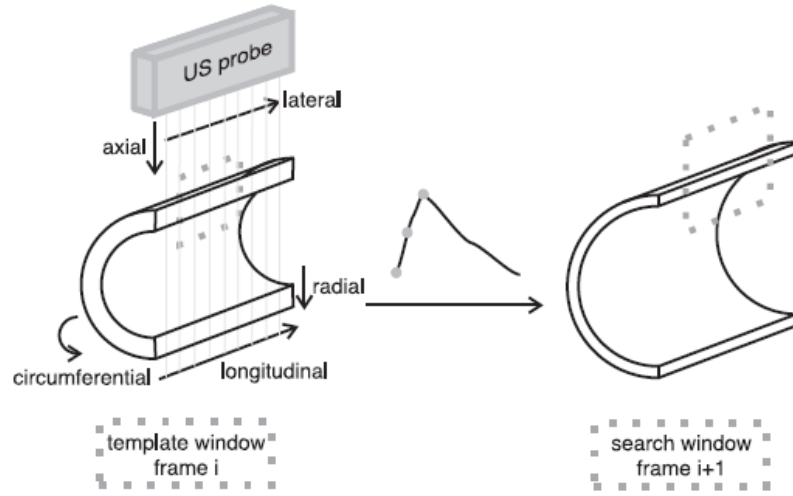


Figure 2.2: An illustration of a vessel before inflation (left) and at maximum inflation (right). The dotted square represents the search window used for the displacement estimation [4]

on these purely geometrical criteria. To develop better treatment criteria to improve patient diagnosis and clinical decision making, patient specific information of the plaque composition and mechanical properties is needed. Only non-invasive techniques would qualify for this purpose, since those techniques can also be used for screening purposes. Different imaging modalities are used to obtain information about geometry and morphology of a plaque in the carotid artery. The most used imaging techniques in medical diagnostics are magnetic resonance imaging (MRI), computed tomography (CT), and ultrasound (US) imaging. Compared to MRI and CT, US imaging has low cost, short scanning time, and no radiation exposure. Therefore, US imaging is the most frequently used imaging modality for screening patients with carotid plaques. Other advantages of US imaging are its high temporal and spatial resolution, and its real-time 2-D and 3-D imaging performance. However, US can not distinguish between or visualize the different plaque components i.e. lipids, calcifications and fibrous tissue. This is possible with MRI, but requires long scanning times and is relatively expensive [39]. Furthermore, US provides a limited field of view and has large inter-observer variability.

Already a lot of research has been performed to obtain mechanical properties of carotid artery using strain imaging techniques or vascular elastography, all based on ultrasound. With ultrasound imaging, the geometry and deformation of the carotid artery can be obtained. In a patient, the geometry of the carotid artery is imaged during the cardiac cycle with a frame rate of 20 - 80 Hz. The displacements of the arterial wall due the intraluminal blood pressure can be estimated. Radio-frequency (RF) data can be used for detailed 2-D strain imaging of local strains within the carotid wall (Ophir et al. [29], Ribbers et al. [30]) or the image (B-mode) data for speckle tracking which yields the global strains in the carotid artery as shown by Golemati et al. [14]. Also intravascular ultrasound (IVUS) elastography techniques have been developed and applied to detect vulnerable plaques in the coronary arteries based on strain data (De Korte et al. [8]). The advantage of using IVUS is that a high spatial resolution is obtained in the radial direction of the vessel, so assessment of radial strains is highly precise and accurate. It was shown that high strains in the shoulders of the coronary plaques correlated to plaque vulnerability (De Korte et al. [8], Schaar et al. [35]). However, for carotid imaging these techniques are too invasive. Non-invasive strain imaging techniques for the carotid artery based on RF-data were developed by Hansen et al. [15], Ribbers et al. [30] and Schmitt et al. [36]. The 2-D strains are estimated in the direction of the ultrasound beam, where the highest precision and resolution is only available in the axial direction. To estimate material properties of the vascular wall, the motion and strain as a response to the intraluminal blood pressure can be analysed (Laurent et al. [23], Benetos et al. [3], Hoeks et al.

[18]). The change in diameter and the pressure are used to calculate the incremental Young's modulus or the distensibility. These methods assume small deformations and linear, isotropic material behavior. Due to the complexity of biological tissue these assumptions are not valid for the entire stress-strain behavior of the arterial tissue (Holzapfel et al. [19]). Vascular elastography is a method where the mechanical properties of the vascular wall, such as the Young modulus, are estimated using ultrasound imaging. The material stiffness is estimated by combining the strain data with the blood pressure and a biomechanical model, using a finite element method (Baldewsing et al. [1], Richards and Doyley [31]). The advantage is that instead of a pressure dependent parameter like strain, a constituent property of the material is estimated. Doyley et al. [11] presents an iterative reconstruction method for spatial distribution of Young's moduli from within soft tissues. They optimize the Young's modulus distribution in a finite element analysis to minimize the differences between experimental and calculated displacements on every node. In the work of Baldewsing et al. [1] (and Baldewsing et al. [2]) an IVUS strain elastogram from a coronary plaque was used to reconstruct the Young's modulus image, a so-called modulogram, of the plaque. The reconstruction is an ill-posed inverse elasticity problem (Hardamar [17]), therefore, spatial a priori information of the plaque's geometry is needed (Le Floc'h et al. [24], Richards and Doyley [32]). In these methods only 2-D geometries are used, since displacements on every node are required, which is not feasible with 3-D US imaging at the desired resolution.

2.2 Goal of this study

In this study, we will estimate patient specific material properties using an inverse approach, which will be tested on artificial vessel and plaque phantoms. A method was developed to estimate the "average" material properties of a large part of the vascular wall, in both homogeneous and heterogeneous vascular phantoms. Here, we will match a finite element model (FEM) with the displacement field measured by US, by updating the material properties of the FEM. Hence, the material properties of a complete part of the material are estimated rather than a Young's modulus distribution. The advantage is that less prior information is needed, since less parameters are calculated. Furthermore, a single (simple) measure for arterial wall stiffness is non-invasively obtained. This methodology could be extended to possibly identify the presence of lipid in the arterial wall. The validation of techniques like vascular elastography is typically performed on phantoms and simulation studies. Cylindrical phantoms are developed, with the same mechanical properties as real vascular tissue. Gelatin phantoms were first used by Ryan and Foster [34] for use in intravascular ultrasound imaging studies. Different geometries can be constructed with different elastic properties. De Korte et al. [9] designed phantoms with a combination of gelatin and agar. The major drawback of agar and gelatin phantoms is the limited shelf life [4]. Therefore, polyvinyl alcohol cryogel (PVA-c) phantoms introduced and have been used to validate e.g. a strain imaging method by Hansen et al. [16]. In this study, PVA-c phantoms were developed with increasing complexity, both in geometry and the number of constituents. In a previous study, Boekhoven et al. [4] developed polyvinyl alcohol (PVA) phantoms that mimic the carotid artery, consisting of multiple layers but also including a lipid inclusion. An experimental set-up was created to perform an inflation experiment and US imaging. The phantom is imaged during the inflation with an ultrasound device. This experiment mimics the imaging of a carotid artery *in vivo*. The inflation experiment is then simulated using finite element analysis: 3-D finite element meshes were constructed from 2-D ultrasound images. In this thesis a complete framework is described, including phantoms construction, inflation testing, US functional imaging, Finite Element Analysis, parameter estimation procedure, and the validation of this method.

Chapter 3

Materials and Methods

In the sections 3.1 to 3.4, the inverse approach to estimate vascular mechanical properties is proposed. The inverse approach is tested in-silico with two test-cases (section 3.5). Next, the inverse approach was tested on carotid phantoms (section 3.6-3.9). Finally, to validate the US-based results, uni-axial tensile testing was performed (section 3.11-3.12).

3.1 The inverse approach

First, a forward problem of an inflation experiment is formulated. In this experiment, a thick-walled tube is pre-stretched in longitudinal direction with λ_z and subsequently inflated with pressure p . The stress-free configuration of the tube is defined by:

$$\Omega(\mathbf{X}_0, \boldsymbol{\sigma}_0) . \quad (3.1)$$

Here, \mathbf{X}_0 is the material coordinates of the undeformed configuration of the tube and $\boldsymbol{\sigma}_0$ the zero-stress state of this configuration. Only residual stresses are present in the tube [13]. The tube is pre-stretched in longitudinal direction. This results in the deformed configuration:

$$\Omega(\mathbf{X}_L, \boldsymbol{\sigma}_L) , \quad (3.2)$$

with \mathbf{X}_L the coordinates of the pre-stretched tube, and $\boldsymbol{\sigma}_L$ the second-order stress tensor. Now a pressure p is applied to the inner surface of the pre-stretched tube. This results in the second deformed configuration:

$$\Omega(\mathbf{X}_p, \boldsymbol{\sigma}_p) , \quad (3.3)$$

in which \mathbf{X}_p denotes the coordinates of the inflated tube and $\boldsymbol{\sigma}_p$ the corresponding stress tensor. The pressure is defined as:

$$p = -\boldsymbol{\tau} \cdot \mathbf{n} = -(\boldsymbol{\sigma} \cdot \mathbf{n}) \cdot \mathbf{n} , \quad (3.4)$$

with \mathbf{n} , the normal unit vector and $\boldsymbol{\tau}$ the traction vector. A material model Ψ is chosen to define a relation between the strain field $\boldsymbol{\epsilon}$ and the stress field $\boldsymbol{\sigma}$.

$$\boldsymbol{\sigma} = \Psi(\boldsymbol{\epsilon}, C) . \quad (3.5)$$

Here, C is a set of material properties corresponding to the chosen material model. A deformed configuration can be calculated from the previous configuration by a forward solver, denoted by \mathcal{S}_L . The analysis from the stress-free configuration to the pre-stretched state is then defined by:

$$\Omega(\mathbf{X}_L, \boldsymbol{\sigma}_L) = \mathcal{S}_L(\Omega(\mathbf{X}_0, \boldsymbol{\sigma}_0), \lambda_z, C) , \quad (3.6)$$

with λ_z the pre-stretch in longitudinal direction defined as:

$$\lambda_z = \frac{L}{L_0} . \quad (3.7)$$

Here, L is the length of the phantom after applying the pre-stretch and L_0 the length corresponding to the stress-free configuration. The deformation gradient tensor \mathbf{F}_L for this step is given by:

$$\mathbf{F}_L = \frac{\partial \mathbf{X}_L}{\partial \mathbf{X}_0}. \quad (3.8)$$

In the second step is the phantom pressurized, the sum from pre-stretched configuration to the pressurized tube is defined by:

$$\Omega(\mathbf{X}_p, \sigma_p) = \mathcal{S}_p(\Omega(\mathbf{X}_L, \sigma_L), p, C). \quad (3.9)$$

The deformation gradient tensor \mathbf{F}_p for this step is given by:

$$\mathbf{F}_p = \frac{\partial \mathbf{X}_p}{\partial \mathbf{X}_L}. \quad (3.10)$$

The deformation gradient tensor \mathbf{F} for both steps combined is:

$$\mathbf{F} = \mathbf{F}_L \cdot \mathbf{F}_p. \quad (3.11)$$

In the inflation experiment the tube is imaged during the second step (\mathcal{S}_p). The pressure is applied from 0 to the maximum pressure p_{max} . If we have a closer look at the variables in the second step (3.9) applied to the inflation experiment:

$$\left\{ \begin{array}{ll} \mathbf{X}_L & \text{Geometry imaged with US: at } p = 0 \text{ and } L = L_0 \cdot \lambda_z \\ \mathbf{X}_p & \text{Geometry imaged with US: at } p = p_{max} \\ \sigma_L & \text{Estimated with backward displacement method [5] (Section 3.2)} \\ p & \text{Measured} \\ \sigma_p & \text{Unknown} \\ C & \text{Unknown} \end{array} \right. \quad (3.12)$$

The stress σ_L can be estimated with the backward displacement method by estimate the stress-free configuration \mathbf{X}_0 and calculate the forward problem \mathcal{S}_L , described in section 3.2. In this experiment the unknown parameters are the material properties C and the stress tensor after applying the internal pressure σ_p . So the forward problem does not apply to this situation where σ_p and \mathbf{X}_p are the unknown parameters. Therefore, an inverse approach can be formulated. The goal is to find the set of material properties C , so that subsequently the forward problem in (3.9) can be solved, which will give σ_p .

Now let C^* be an initial guess for the material properties:

$$\Omega(\mathbf{X}_p^*, \sigma_p^*) = \mathcal{S}_p(\Omega(\mathbf{X}_L, \sigma_L), p, C^*). \quad (3.13)$$

Here, \mathbf{X}_p^* is the estimated deformed configuration after applying the pressure with material properties C^* . σ_p^* is the corresponding stress tensor. Since \mathbf{X}_p is already known, the difference between the estimated and known configuration can be quantified as the root mean squared error of the displacements:

$$\mathcal{E} = \frac{1}{N} \sum^N |\mathbf{X}_p - \mathbf{X}_p^*|. \quad (3.14)$$

Here, \mathcal{E} is a measure for the error between the estimated configuration \mathbf{X}_p^* and the imaged configuration \mathbf{X}_p and N represents the number of nodes in the model. When

$$\mathbf{X}_p^* = \mathbf{X}_p \quad (3.15)$$

this would imply that:

$$\left\{ \begin{array}{l} \sigma_p = \sigma_p^* \\ C = C^* \end{array} \right. \quad (3.16)$$

So, to find this configuration \mathbf{X}_p^* , an algorithm \mathcal{A} is developed which minimizes the error \mathcal{E} by varying the material properties C^* :

$$\mathcal{A} = \min(\mathcal{E}(C^*)). \quad (3.17)$$

In this thesis, such an optimization algorithm is developed and applied to determine material properties of a vascular phantom.

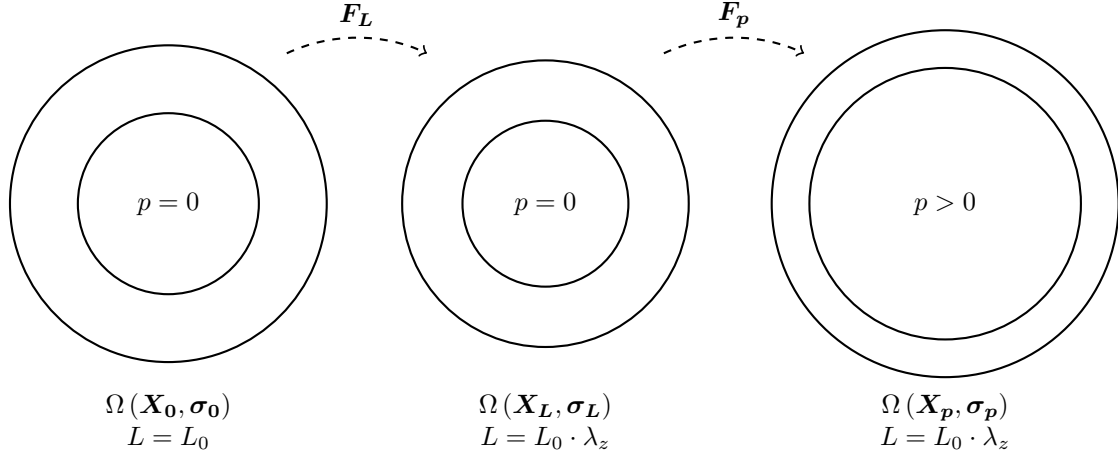


Figure 3.1: The three different configurations of the tube in the inflation experiment.

3.2 Backward displacement method

To solve for \mathcal{S}_p in equation 3.9, the stress tensor σ_L should be known. This tensor could be calculated by solving the problem \mathcal{S}_L in equation 3.6, however, the stretch-free configuration \mathbf{X}_0 is unknown. This configuration could be derived from the dimensions of the mold or by imaging the stress-free configuration. To calculate σ_L we can solve the following problem:

$$\Omega(\mathbf{X}_L^*, \sigma_L^*) = \mathcal{S}_L(\Omega(\mathbf{X}_0, \sigma_0), \lambda_z), \quad (3.18)$$

the longitudinal pre-stretch λ_z is measured during the experiment. The stress σ_0 is assumed to be zero, so residual stresses are neglected, since a small opening angle was measured for the PVA phantom. Summarizing:

$$\begin{cases} \mathbf{X}_0 & \text{Based on the geometry of the mold or obtained from imaging.} \\ \sigma_0 & 0 \\ \lambda_z & \text{Measured} \\ \sigma_L^* & \text{Unknown} \\ \mathbf{X}_L^* & \text{Unknown (in this problem)} \end{cases} \quad (3.19)$$

It turned out that the calculated configuration \mathbf{X}_L^* was not equal to the measured configuration \mathbf{X}_L . A combination of explanations is possible (see section 5.3). By applying this method, the displacement matching between the measured and the simulated configuration (to calculate \mathcal{E}) will be complicated.

Hence, to overcome these problems, the backward displacement method described by Bols et al. [5] was used. In this paper, the undeformed configuration of a thick-walled tube at $p = 0$ is estimated from a measured configuration with $p > 0$ using this method. Here, the backward displacement method was adjusted to estimate the undeformed configuration \mathbf{X}_0 with $L = L_0$ from the measured configuration \mathbf{X}_L with $L = L_0 \cdot \lambda_z$. To explain the method, we consider the following problem:

$$\Omega(\mathbf{X}_L, \sigma_L^*) = \mathcal{S}_L(\Omega(\mathbf{X}_0^*, \sigma_0), \lambda_z) \quad (3.20)$$

with,

$$\begin{cases} \mathbf{X}_L & \text{Geometry imaged with US: at } p = 0 \\ \sigma_0 & 0 \text{ (assume residual stress is zero)} \\ \lambda_z & \text{Measured} \\ \mathbf{X}_0^* & \text{Unknown} \\ \sigma_L^* & \text{Unknown} \end{cases} \quad (3.21)$$

Again, this is not a forward problem. The stress-free configuration \mathbf{X}_0^* and the stress tensor σ_L^* are the unknown parameters. The deformation from the stress-free configuration \mathbf{X}_0^* to the pre-stretched configuration \mathbf{X}_L can be described with the mapping function Φ : $\mathbf{X}_0^* \mapsto \mathbf{X}_L$.

$$\mathbf{X}_L = \Phi(\mathbf{X}_0^*) . \quad (3.22)$$

The un-stretched reference geometry can be determined with the inverse mapping function Φ^{-1}

$$\mathbf{X}_0^* = \Phi^{-1}(\mathbf{X}_L) . \quad (3.23)$$

This allows to obtain the un-stretched geometry \mathbf{X}_0^* from the pre-stretched measured geometry \mathbf{X}_L :

$$\Phi(\mathbf{X}_0^*) = \Phi(\Phi^{-1}(\mathbf{X}_L)) = \mathbf{X}_L . \quad (3.24)$$

The backward displacement method, described in algorithm 1, is used to solve for the zero-stress geometry by means of fixed points iterations. It starts with a forward problem, where the measured geometry is stretched in longitudinal direction with u_z , so that $L = L_0 + u_z$. The obtained displacements of every node are used to calculate the new geometry X^{i+1} , so the nodal coordinates of the mesh are updated every iteration.

Algorithm 1: The backward displacement method developed by Bols et al. [5], used to recover the geometry without pre-stretch (\mathbf{X}_0).

```

1 i = 0
2  $\mathbf{X}^i = \mathbf{X}_L$ 
3 while  $r_{max} < \epsilon$  do
4   i = i + 1
5    $\Omega(\mathbf{x}^i, \sigma^i) = \mathcal{S}_L(\Omega(\mathbf{X}^i, 0), u_z)$ :
6    $\mathbf{U}^i = \mathbf{x}^i - \mathbf{X}^i$ 
7    $\mathbf{X}^{i+1} = \mathbf{X}_L - \mathbf{U}^i$ 
8 end
9  $\mathbf{X}_0 = \mathbf{X}^i$ 
10  $\sigma_L = \sigma^i$ 
    
```

To measure the convergence of the backward displacement method, the residual r_j^i is calculated for every node:

$$r_j^i = \|\mathbf{X}_{L,j} - \mathbf{x}_j^i\|, \quad j \in [1, N] . \quad (3.25)$$

Here, r_j^i is the distance between the coordinates of the j th node of the i th pre-stretched geometry and the measured geometry \mathbf{X}_L .

$$r_{max}^i = \max(r_j^i), \quad j \in [1, N] \quad (3.26)$$

When the maximum distance r_{max}^i is smaller than the convergence criterion ϵ , the search is terminated.

3.3 Optimization algorithm

An optimization algorithm \mathcal{A} (3.17) was adapted to estimate material properties by minimizing the error \mathcal{E} , as described in equation 3.14. This algorithm should return the actual material properties by minimizing the differences between the simulated displacements (U_{FEM}) and the reference displacements from the inflation experiment (U_{REF}). Different from equation 3.14, only displacements in a 2-D plane are compared, the 2-D plane imaged with ultrasound. To have a measurement for those differences, the mean root squared error E is defined in equation 3.27. E is the absolute average error between the displacements U_{FEM} and U_{REF} :

$$E = \frac{1}{n} \sum^n |U_{REF} - U_{FEM}| . \quad (3.27)$$

Here, n is the number of tracking points. So the optimization algorithm \mathcal{A} minimizes E . Let f be a function that first solves problem \mathcal{S}_L (pre-stretch the tube) and subsequently solves the problem \mathcal{S}_p (inflation of the tube) with material properties G :

$$E(G_1, \dots, G_k) = f(G_1, \dots, G_k) \quad (3.28)$$

Here, k is the number of different material properties to be estimated. The output of this function is the corresponding error E , which should be minimized. Two different optimization algorithms are developed: one for the single layer phantoms where only one material property G is estimated, and an algorithm for the double layer and plaque phantoms where two different shear moduli G_i and G_o are estimated. Two different optimizations algorithms are used: Golden section search for $k = 1$ and the Downhill simplex method for $k = 2+$.

3.3.1 Golden section search

To find the minimum error E for a single layer phantom the Golden section search was used. This algorithm is used to find an extreme value, in this case a minimum, of an uni-modal function [22]. The first step is to find an interval wherein a minimum exists. Next, the minimum can be obtained by narrowing the search range for every iteration. In figure 3.2, the minimum is bracketed between the points x_1 and x_3 (In our case x can be replaced for a value for G). The function f is evaluated at x_4 . If $f_4 > f_2$ than the new brackets are x_1 and x_4 . When $f_2 > f_4$ the new brackets are x_2 and x_3 . Every new point to be evaluated is based on the golden ratio:

$$\frac{c}{a} = \frac{a}{b} = \frac{1}{\phi}, \quad (3.29)$$

where ϕ is the golden ratio:

$$\phi = \frac{1 + \sqrt{5}}{2} = 1.618 \quad (3.30)$$

For every iteration, the search domain is decreased in size. The minimum is found when $c < \epsilon$, with ϵ the stop criterion.

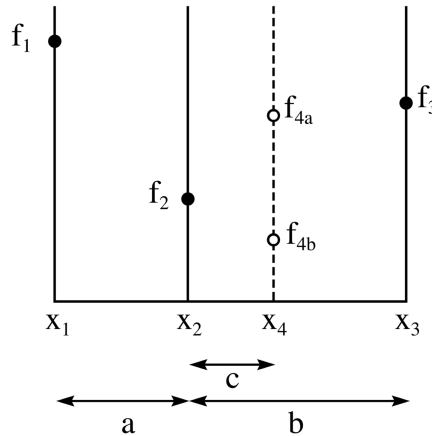


Figure 3.2: An illustration of the Golden Section Search. Image from wikipedia.org.

3.3.2 Downhill simplex method

The Downhill simplex method, also known as Nelder-Mead method, is used to find the maximum or minimum value for a non-linear function, for which the derivatives are unknown [28]. An advantage of this method is that it's computational cost is quite low. It follows a set of rules

to move a simplex over an N -dimensional landscape. A simplex is a polytope in N dimensions with $N + 1$ vertices, in 2-D it is a triangle and in 3-D a tetrahedron. The moves allowed of the simplex are reflection, expansion, contraction and shrinkage. Figure 3.3 shows the movements for a simplex in 2-D [22]. The magnitude of the movements are controlled by d , the distance from the vertex with the highest value to the opposing centroid. In the situation of the double layered phantom, there are two unknown material properties, G_i for the inner layer and G_o for the outer layer. The function f is evaluated for different values of G_o , G_i . The simplex 'moves' over the solution field away from the highest value in the simplex. A summary of this method is given in Algorithm 2. After the function converged to a minimum the coordinates of the lowest vertex are the corresponding values for G_o and G_i .

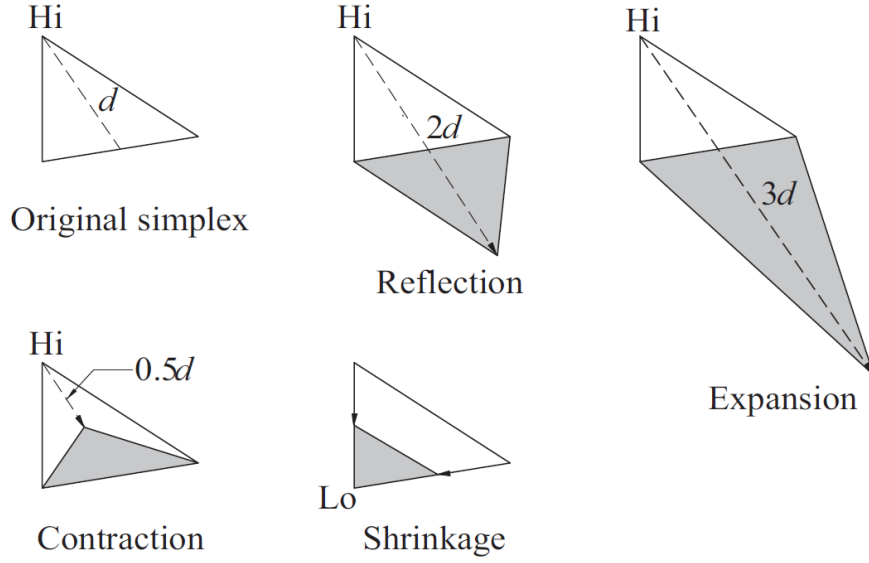


Figure 3.3: Different moves for a simplex in the Downhill simplex method [22].

Algorithm 2: A Summary of the downhill simplex algorithm that minimizes the function f . The goal is to find a set of material properties G at $\min(f(G))$.

```

1 Initialization:
2 while  $E < tol$  do
3   Calculate initial simplex:  $Low = \min(f(G))$  and  $Hi = \max(f(G))$  and
    $Sec = \text{second max}(f(G))$ 
4   try reflection with  $G_{refl}$ 
5   if  $f(G_{refl}) < Low$  then
6     accept reflection
7     try expansion with  $G_{exp}$ 
8     if  $f(G_{exp}) < Hi$  then
9       accept expansion
10    end
11  else
12    try reflection again
13    if  $f(G_{refl}) \leq Sec$  then
14      accept reflection
15    else
16      if  $f(G_{refl}) \leq Hi$  then
17        accept reflection
18      end
19      try contraction with  $G_{con}$ 
20      if  $f(G_{con}) \leq Hi$  then
21        accept contraction
22      else
23        use shrinkage
24      end
25    end
26  end
27 end
28  $G = Low$ 
    
```

3.4 Finite element analysis

Both formulated forward problems, \mathcal{S}_L (3.6) and \mathcal{S}_p (3.9), are solved with ABAQUS using finite element analysis. The meshed geometry \mathbf{X}_L is obtained from the US data. The stress-free configuration \mathbf{X}_0 is determined with the backward displacement method. To describe the material behavior of PVA the neo-Hookean material model is assigned. The neo-Hookean model is a hyperelastic material model which can be used for predicting stress-strain behavior of linear-elastic materials undergoing large deformations (i.e., geometrically non-linear). The constitutive equation for a neo-Hookean incompressible solid is given by:

$$\boldsymbol{\sigma} = -p\mathbf{I} + G(\mathbf{B} - \mathbf{1}) , \quad (3.31)$$

with the finger deformation or left Cauchy-Green tensor \mathbf{B}

$$\mathbf{B} = \mathbf{F}\mathbf{F}^T . \quad (3.32)$$

Here, \mathbf{F} is the gradient deformation tensor. The strain-energy density function for a neo-Hookean solid is given by:

$$\Psi = \frac{G}{2}(I_1 - 3) , \quad (3.33)$$

with G the shear modulus and I_1 the first invariant of \mathbf{B} :

$$I_1 = \text{tr}(\mathbf{B}) = \lambda_1^2 + \lambda_2^2 + \lambda_3^2 . \quad (3.34)$$

The neo-Hookean material model only has one material property, the shear modulus G . The Bulk modulus D is set to $1 \cdot 10^{-5}$, so that the material behaves incompressible. For the double layer phantom, two different material parameters are assigned, one for the inner wall and outer wall. Two different sums were performed. In the backward displacement method the sum \mathcal{S}_L was solved iteratively, to obtain the initial geometry \mathbf{X}_0 . In the inverse approach both \mathcal{S}_L and \mathcal{S}_p combined were solved iteratively. First, the tube is pre-stretched with u_z to obtain \mathbf{X}_L with the corresponding stress tensor $\boldsymbol{\sigma}_L$. Next, the pressure p is applied to the inside (lumen) wall of the phantom. The tube is inflated from 0 to 100 mmHg, adjusted if necessary to the actual pressure signal values measured during the experiment. During the inflation of the FE model, both sides of the tube are restricted to move, similar to the inflation experiment. Now U_{FEM} can be obtained, the displacements of the wall in radial direction. ABAQUS and calculation of the error (equation 3.27) were executed via a custom Python script. With the optimization methods included in this script, a new material property (G) was assigned to the mesh iteratively.

3.5 In Silico Testing

3.5.1 Test Case: Optimization Algorithm

In this test case the performance of the optimization algorithm was tested for different geometries and initial values for the material properties. First, eight different tubes were created in ABAQUS, with the same dimensions as the phantoms. The dimensions are displayed in table 3.1. To obtain the reference displacements (U_{REF}) the tubes were pressurized with known material properties. In this case, an optimal solution exists where the error between the FEM displacements (U_{FEM}) and the reference displacements is equal to zero. To test if the optimization algorithm is able to minimize the error E , simulations were performed with 16 different start positions for each geometry. The results are displayed in table 4.1.

Table 3.1: Dimensions of different tubes. l = length of tube, l_{sten} = length of stenosis, r_{lum} = radius of lumen, r_{sten} = radius of lumen at maximum stenosis, wt_{inner} = wall thickness of the inner layer, wt_{outer} = wall thickness of the outer layer and d = total diameter of the tube. All units are given in millimeters.

Tube geometry [mm]	l	l_{sten}	r_{lum}	r_{sten}	wt_{inner}	wt_{outer}	d
single layer	32	0	2.5	2.5	1.5	0	8
single layer 20% stenosis	32	16	2.5	2	1.5	0	8
single layer 40% stenosis	32	16	2.5	1.5	1.5	0	8
single layer 60% stenosis	32	16	2.5	1	1.5	0	8
double layer	32	0	2.5	2.5	0.50	1	8
double layer 20% stenosis	32	16	2.5	2	0.50	1	8
double layer 40% stenosis	32	16	2.5	1.5	0.50	1	8
double layer 60% stenosis	32	16	2.5	1	0.50	1	8

3.5.2 Test Case: Influence of noise

The reference displacements will always contain a certain level of noise due to the ultrasound imaging and the displacement tracking. To get a general idea of the influence of noise on the accuracy of the material property estimation a second test case was developed. A single layer tube with 40% stenosis was created in ABAQUS. Material properties are assigned to the tube, $G = 50$ kPa. The tube was pressurized from 0 to 100 mmHg and the reference displacement field was obtained. Gaussian noise was added to the reference displacements, see equation 3.35.

$$U_{REF,i} = U_{REF,i} + g(0, \alpha \cdot U_{REF,i}) \quad (3.35)$$

Here is g the probability density function for the Gaussian distribution:

$$g(x|\mu, \sigma) = \frac{1}{\sqrt{2\pi}\sigma} e^{-\frac{(x-\mu)^2}{2\sigma^2}} \quad (3.36)$$

where μ is the mean and σ the standard deviation. By variations in α , different levels of noise can be simulated. Next, the optimization is used to estimate the material property G , based on the reference displacements with Gaussian noise. Four different noise levels were applied, for each noise level 10 simulations were performed.

3.6 PVA Phantoms

Polyvinyl alcohol cryogel (PVA-C) phantoms were designed to mimic carotid arteries. The advantage of using a phantom is that the geometry, the number of layers and the stiffness of each layer can be controlled. PVA is a hydrophilic, synthetic polymer. The stiffness of the phantom is determined by the PVA concentration and the number of freeze/thaw cycles (f/t cycles). The phantoms were constructed according to the work by Boekhoven et al. [4]. A complete protocol for PVA preparation can be found in the Appendix.

3.6.1 PVA preparation

Polyvinyl alcohol (PVA) was used. (Mowiol 28-99, Sigma-Aldrich), with Mw 145,000, 99.0-99.8 mol% hydrolysis. A solution of 15 wt% PVA in demineralized water was prepared with 1 wt% of ultrasound scatterers (Orgasol 2001, Arkema France), which have an average size of $5.8 \mu m$. The solution was heated at approximately $85^\circ C$ and stirred with a magnetic stir bean for 4 hours. After another 4 hours of cooling down at room temperature ($\pm 25^\circ C$), the PVA gel was ready to pour into the molds.

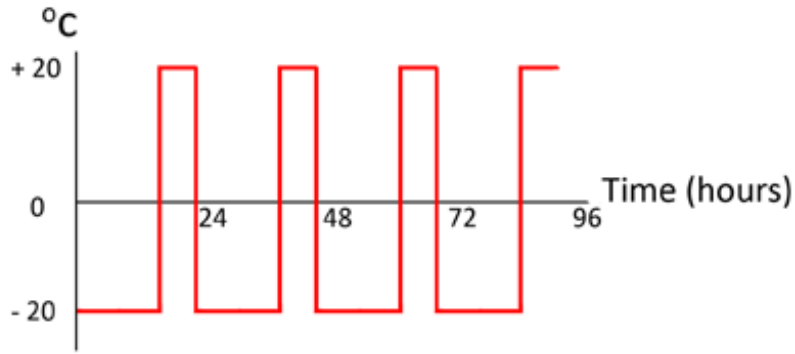


Figure 3.4: Overview of four freeze-thaw cycles of 16 hours freezing and 8 hours thawing.

3.6.2 Phantom preparation

Phantoms with different geometries were constructed using axi-symmetric phantom molds. The outside of the mold is a tube of Perspex. A stainless steel bar was used to create the lumen. To create phantoms with a stenosis, the steel bar has a smaller diameter towards the middle. Single layer phantoms were subjected to four freeze/thaw cycles. One cycle consists of 16 hours of freezing at $-20^\circ C$ and 8 hours of thawing at room temperature, as illustrated in Figure 3.4. The double layer phantoms were constructed from the outer layer to the inner layer, resulting in a stiff outer layer and a less stiff inner layer. This is in agreement with the *in vivo* situation, where the inner layer (intima) of an artery is less stiff than the outer layer (adventitia). The outer layer first underwent two f/t cycles. Next, a smaller mold was used and PVA-gel was injected into the tube

to create the inner layer. After that the phantom was subjected to another two cycles. When the molds are removed, the phantoms can be preserved in purified water at 5 °C for years. Table 3.2 shows an overview of the dimensions of the constructed phantoms.

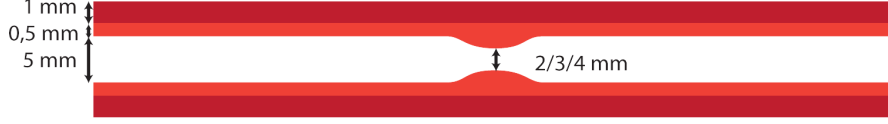


Figure 3.5: Composition of a double layer phantom with stenosis.

Table 3.2: The dimensions of the different constructed phantoms. All phantoms have a normal inner diameter of 5 mm whereas $D_{stenosis}$ is the inner diameter at the location of the stenosis. The length of the tubes is 5 cm. The wall thickness of the single layer phantoms is 1.5 mm. The double layer phantoms have a wall thickness in the inner layer of 0.5 mm and the outer layer 1.0 mm.

Geometry	$D_{stenosis}$
Single layer 0% stenosis	5 mm
Single layer 20% stenosis	4 mm
Single layer 40% stenosis	3 mm
Single layer 60% stenosis	2 mm
Double layer 0% stenosis	5 mm
Double layer 20% stenosis	4 mm
Double layer 40% stenosis	3 mm
Double layer 60% stenosis	2 mm

3.7 Inflation experiment

To simulate the deformation of a pulsating carotid, an experimental set-up developed by Van den Broek et al. [38] is used. This set-up consists of an organ bath and a set of tubes connected to a pump. The phantom can be mounted between two stainless steel tubes in the organ bath. The phantom is stretched in longitudinal direction, with approximately $\lambda_z = 1.2$. The pump is controlled with LabView (National Instruments, Texas, USA), the pulsation frequency and the pulsation strength can be set to the desired values. Between the pump and the steel tube a pressure sensor is connected. The organ bath is filled with water and the ultrasonic probe is placed above the phantom in longitudinal direction. The pulsation frequency is set to 1 Hz (60 bpm) and the pressure strength is adjusted so that the measured pressure difference ($p_{max} - p_{min}$) is equal to 100 mmHg. With a diastolic pressure of 0 mmHg. A zero-pressure reference was used to obtain the full pressure-diameter behavior of the phantoms. Ultrasound imaging was performed with a MyLab70 ultrasound system (ESAOTE EUROPE, NL) equipped with a linear array probe, recording 62 frames/s in 2-D B-mode. For every phantom 4 pulsation cycles are imaged. The RF data and the pressure data were used for further analysis.

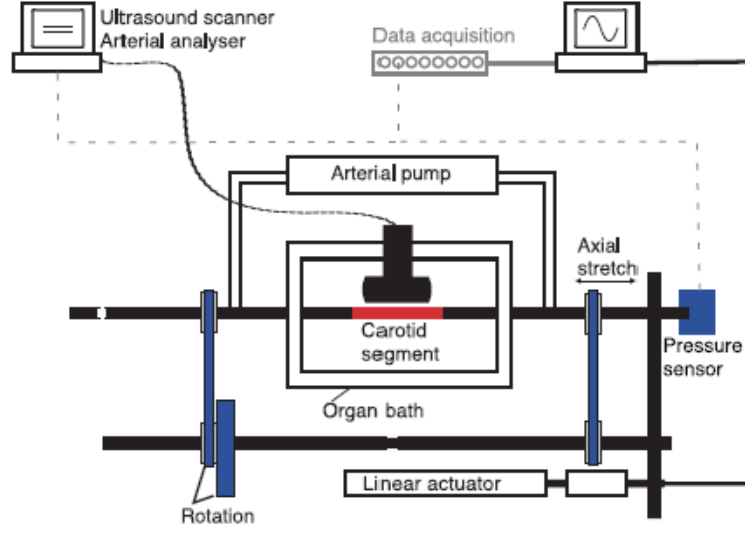


Figure 3.6: Overview of the experimental set-up of the inflation experiment [4].

3.8 Displacement tracking

The RF data obtained from the inflation experiment were imported in MATLAB (MATHworks, Natick, MA, USA). The data is analysed with in-house software. To obtain a geometry for further analysis segmentation of the data is necessary. First the frames of one single pulse were selected in M-mode, from the minimum to the maximum diameter of the phantom. The frame selection is shown in Figure 3.7, the frames between the red lines are selected. The corresponding pressure signal was obtained from the pressure data. In a B-mode image the luminal wall and the outer wall were segmented manually. Between the segmentation lines a grid of tracking points was constructed. To estimate the displacements of the wall a 2-D iterative coarse-to-fine method was used [25]. In the first step, coarse displacements are estimated from large segments of detected US-data using only the signal envelope. In the second step, these displacements are used as initial guess for the second cross-correlation step with a smaller window [7]. During the inflation there are approximately zero displacements in longitudinal direction. If the tube is aligned with the x-axis of the US image, the vessel expands in the radial direction, which now coincide with the axial direction. Hence, to improve the displacement estimation, motion was only estimated in the axial direction. After this step the displacements were filtered with a median filter (11 by 11 pixels). It was noticed that the displacements at the luminal wall were underestimated due to the presence of air bubbles in the lumen. Therefore, the filter size in radial direction was reduced from 11 pixels to 5 pixels.

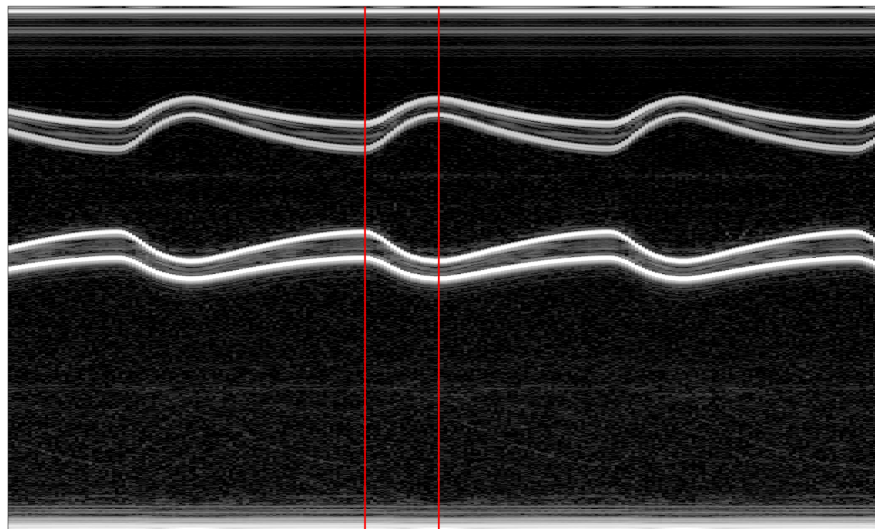


Figure 3.7: M-mode image, the time frames between the red lines are selected for displacement tracking.

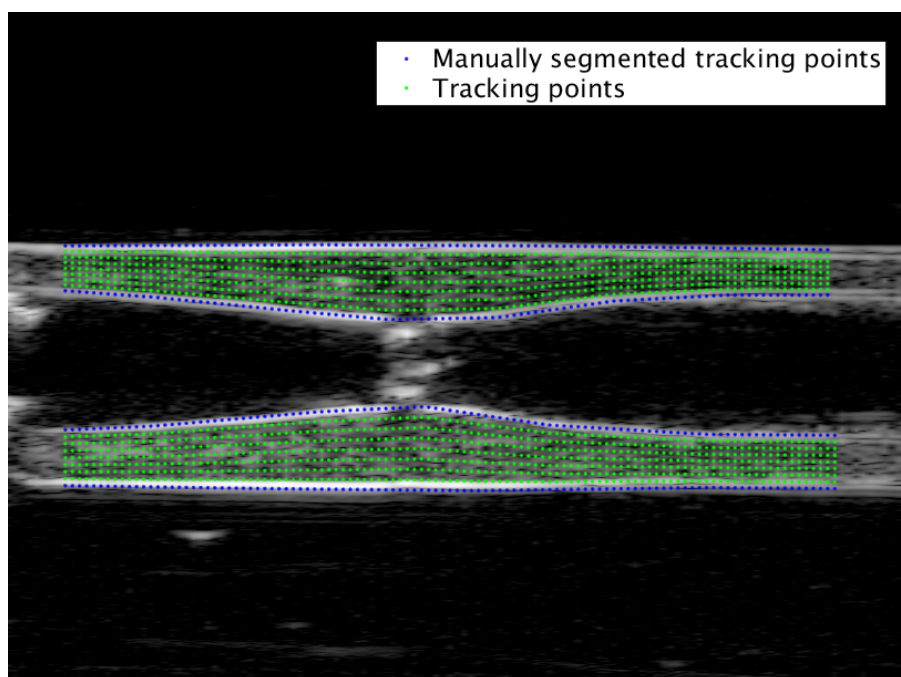


Figure 3.8: B-mode image, showing the tracking points.

3.9 3-D FE meshing using 2-D US-data

The first frame of the selected data was used to obtain the initial geometry, with $p = 0$. Note that this image does not represent the stress-free configuration of the phantom, since the phantom is imaged after a longitudinal pre-stretch had been applied. The phantom molds are circular, therefore it is assumed that a 3-D geometry can be constructed by drawing circles through two points from the lower and upper wall. So, two corresponding tracking points are connected by a circle with a diameter equal to the distance between the two points. If the image acquired with US did not contain the complete tube, the contours are extended on both sides based on the length of the phantom manually measured during the experiment. From the constructed contours a 3-D mesh was generated with TetGen, a tetrahedral mesh generator [37]. In the circumferential direction 36 elements were prescribed and in the radial direction at least 2 elements in each layer were used. Every tracking point will be a node in this mesh. This results in straight-forward matching between the displacements of the FEM and the displacements of the ultrasound tracking.

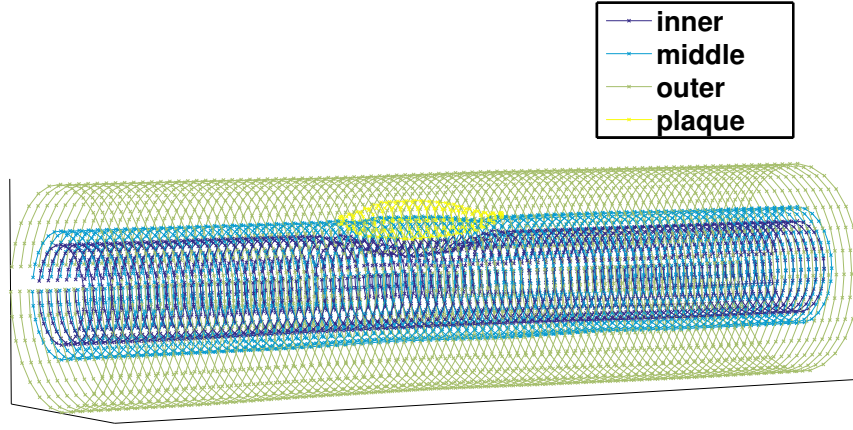


Figure 3.9: Contours of a phantom with a fatty plaque.

3.10 Summary framework

The complete framework can be summarized as:

1. Phantoms are constructed.
2. Inflation experiment and US imaging of the phantom is performed.
3. A mesh is generated from the ultrasound data \mathbf{X}_L and the reference displacements U_{REF} are obtained.
4. The initial geometry \mathbf{X}_0 is estimated with the backward displacement method.
5. An initial guess for the material properties is used to solve the sum where \mathbf{X}_0 is stretched with displacement u_z and subsequently is pressurized with pressure p . The displacements in a 2-D plane U_{FEM} are obtained.
6. The error between the displacements U_{FEM} and U_{REF} (eq. 3.27) was calculated and evaluated. The optimization method returns new material properties for the simulation in step 6. Step 6 and 7 are repeated until the convergence criteria is reached.
7. The material properties G_{FEM} of the phantom are estimated with an inverse approach.

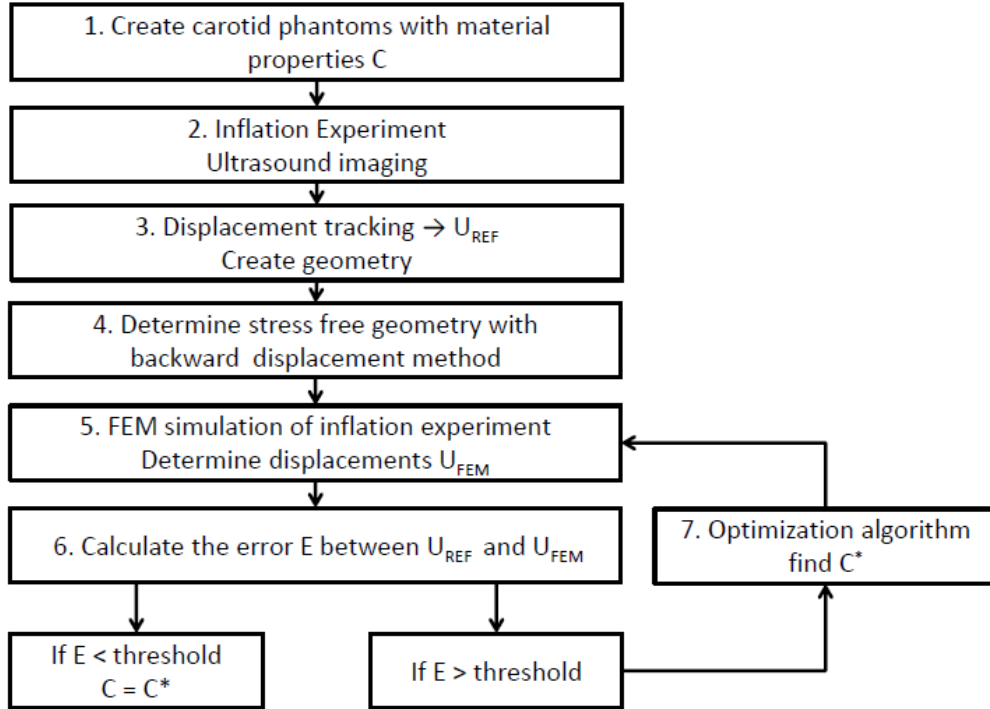


Figure 3.10: An overview of the inverse approach presented in this thesis.

3.11 Uni-axial tensile test

To validate the inverse approach, the mechanical properties of the PVA have to be determined with a different measurement technique. In this study, during the PVA preparation a squared mold was filled with PVA and closed with Plexiglas, for more details see Figure 6.1. Similar freeze-thaw cycles as for the phantoms were applied to the PVA, in order to obtain identical mechanical properties of the phantoms and the tensile test specimen. To create specimens with standard dimensions, a cutting tool was constructed that cuts rectangles with dimensions 30 by 10 mm. The thickness of the specimen is 1 mm. To determine the stiffness of the PVA, uni-axial tensile tests were performed with the Zwick uni-axial tensile testing device (Zwick, Ulm, Germany) with a 20N load cell. The tensile tests were performed with a constant speed of 30 mm/min until the specimen either brakes or releases from the clamps.

3.11.1 Equations uni-axial tensile test

If incompressibility is assumed and the specimen is stretched in the y -direction with λ_{yy} , the deformation tensor \mathbf{F} is given by:

$$\mathbf{F} = \begin{bmatrix} \frac{1}{\sqrt{\lambda_{yy}}} & 0 & 0 \\ 0 & \lambda_{yy} & 0 \\ 0 & 0 & \frac{1}{\sqrt{\lambda_{yy}}} \end{bmatrix}. \quad (3.37)$$

The stretch λ_{yy} in the tensile direction is defined by:

$$\lambda_{yy} = \frac{L}{L_0}, \quad (3.38)$$

with L_0 the original length of the specimen and L the current length after applying a tensile force. The neo-Hookean material model is used. Combining equations 3.31 and 3.37 results in an expression for the stress in the tensile direction (σ_{yy}):

$$\sigma_{yy} = -p_0 + G(\lambda_{yy}^2 - 1). \quad (3.39)$$

An expression for the pressure p_0 can be derived by assume plane stress, so the stress in the x -direction σ_{xx} is equal to zero:

$$\sigma_{xx} = -p_0 + G\left(\frac{1}{\lambda_{yy}} - 1\right), \quad (3.40)$$

with $\sigma_{xx} = 0$:

$$p_0 = G\left(\frac{1}{\lambda_{yy}} - 1\right). \quad (3.41)$$

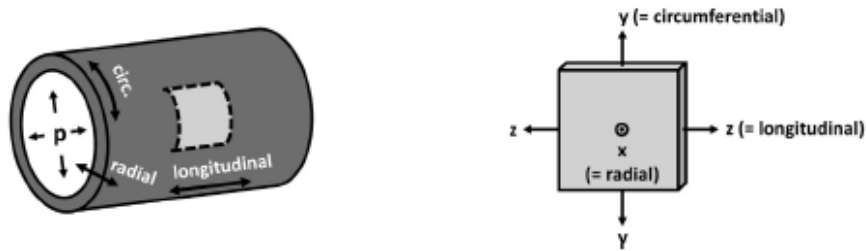
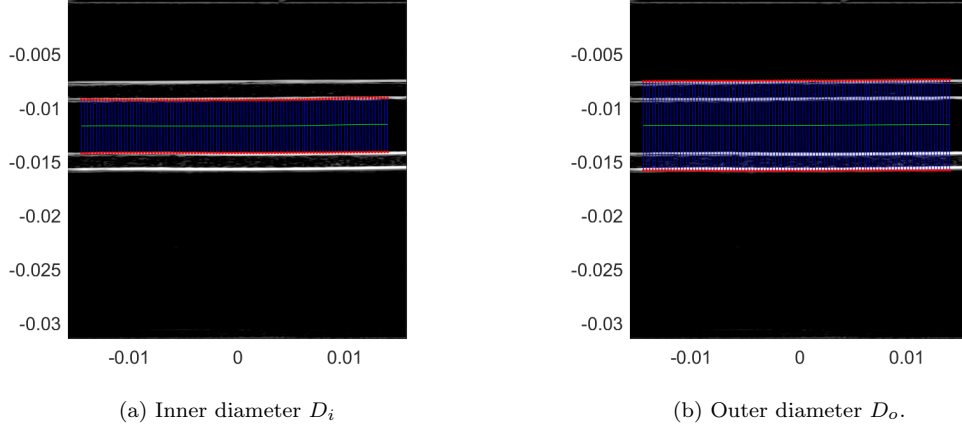


Figure 3.11: Coordinate systems for the inflation experiment (left) and the uni-axial tensile test (right).

[26]



Finally, combining equations 3.39 and 3.41 results in a expression for σ_{yy} :

$$\sigma_{yy} = G \left(\lambda_{yy}^2 - \frac{1}{\lambda_{yy}} \right) . \quad (3.42)$$

3.11.2 Equations inflation experiment

We want to compare the results of the uni-axial tensile test with the inflation experiment. A similar approach was chosen as described in a study by Lopata et al. [26]. In this paper a bi-axial tensile test and an inflation experiment were compared. In the inflation experiment is the phantom pre-stretched in the longitudinal direction with λ_{zz} . If incompressibility is assumed, the corresponding deformation tensor is given by:

$$\mathbf{F}_{0 \rightarrow 1} = \begin{bmatrix} \frac{1}{\sqrt{\lambda_{zz}}} & 0 & 0 \\ 0 & \frac{1}{\sqrt{\lambda_{zz}}} & 0 \\ 0 & 0 & \lambda_{zz} \end{bmatrix} . \quad (3.43)$$

Subsequently, the phantom is inflated with pressure hydrostatic p :

$$\mathbf{F}_{1 \rightarrow 2} = \begin{bmatrix} \frac{1}{\lambda_{\theta\theta}} & 0 & 0 \\ 0 & \lambda_{\theta\theta} & 0 \\ 0 & 0 & 1 \end{bmatrix} \quad (3.44)$$

Here is $\lambda_{\theta\theta}$ the stretch in the circumferential direction defined by:

$$\lambda_{\theta\theta} = \frac{d_p}{d_1} . \quad (3.45)$$

Here d_1 , is the diameter after applying the pre-stretch and d_p is the pressure-dependent diameter. The phantoms are thick-walled tubes, so the diameter in the middle of the wall is used:

$$D_m = \frac{D_o^j + D_i^j}{2} . \quad (3.46)$$

Here is D_o^j (Figure 3.12b) the outer wall diameter on every j th tracking position in longitudinal direction and D_i^j (Figure 3.12a) the diameter of the inner wall on every j th tracking position in longitudinal direction.

To calculate the used diameter d :

$$d = \text{mean}(D_m) . \quad (3.47)$$

The deformation tensor for the complete inflation experiment is:

$$\mathbf{F}_{0 \rightarrow 2} = \mathbf{F}_{0 \rightarrow 1} \cdot \mathbf{F}_{1 \rightarrow 2} = \begin{bmatrix} \frac{1}{\lambda_{\theta\theta}\sqrt{\lambda_{zz}}} & 0 & 0 \\ 0 & \frac{\lambda_{\theta\theta}}{\sqrt{\lambda_{zz}}} & 0 \\ 0 & 0 & \lambda_{zz} \end{bmatrix}. \quad (3.48)$$

The stress in the circumferential direction is given by:

$$\sigma_{\theta\theta,0 \rightarrow 2} = -p_0 + G \left(\frac{\lambda_{\theta\theta}^2}{\lambda_{zz}} - 1 \right) \quad (3.49)$$

Similar to the uni-axial tensile test, it is assumed that there is no plane stress. So the stress in the radial direction is zero, combining this with equation 3.31 results in an expression for the pressure p_0 :

$$p_0 = G \left(\frac{1}{\lambda_{\theta\theta}^2 \lambda_{zz}} - 1 \right). \quad (3.50)$$

Combining equations 3.49 and 3.50 results in an expression for the circumferential stress:

$$\sigma_{\theta\theta} = \frac{G}{\lambda_{zz}} \left(\lambda_{\theta\theta}^2 - \frac{1}{\lambda_{\theta\theta}^2} \right) \quad (3.51)$$

3.12 Inflation test vs uni-axial tensile test

The Neo-hookean model does not describe the material behaviour accurately. Therefore, the comparison between the shear moduli found with the inverse approach and the tensile test is not straight-forward. In this study, it was chosen to compare the material properties in a certain strain range. The Finger strain [21] is defined as:

$$\epsilon_f = \frac{1}{2} (\mathbf{B} - \mathbf{I}). \quad (3.52)$$

The finger strain in circumferential direction in the inflation experiment:

$$\epsilon_{f,\theta} = \frac{1}{2 \cdot \lambda_{zz}} \left(\lambda_{\theta\theta}^2 - \frac{1}{\lambda_{\theta\theta}^2} \right), \quad (3.53)$$

is compared with the finger strain in the tensile direction of the uni-axial tensile test:

$$\epsilon_{f,y} = \frac{1}{2} \left(\lambda_{yy}^2 - \frac{1}{\lambda_{yy}} \right). \quad (3.54)$$

From the inflation experiment $\epsilon_{f,\theta}$ is determined based on the ultrasound images. The same domain of the finger strain $\epsilon_{f,y}$ in the tensile test is used to calculate G_{TT} . This is done for every phantom separately, since $\epsilon_{f,\theta}$ is different for every phantom.

Chapter 4

Results

4.1 In Silico testing

To test the optimization algorithm, a test case was developed, described in section 3.5. The results are displayed in table 4.1. The optimization algorithm always finds the global minimum for the single layer tubes with one unknown material property. For the double layer tubes with two unknown material properties, the optimization algorithm only finds the global minimum for tubes with a certain degree of stenosis. For the double layered straight tube the minimum is only found in 4 out of 16 simulations. Depending on the chosen start position it will find a local minimum. In figure 4.1 the results are shown for the second test case. Here, Gaussian noise was added to a reference displacement field of an inflated tube with shear modulus $G = 50 \text{ kPa}$. The estimated shear moduli are all close to 50 kPa . Even with high noise, $\sigma = 0.4 \cdot U_{REF}$, the average estimated shear modulus is 50.8 kPa .

Table 4.1: Results test case optimization algorithm.

Geometry	Success rate
Single layer 0% stenosis	16/16
Single layer 20% stenosis	16/16
Single layer 40% stenosis	16/16
Single layer 60% stenosis	16/16
Double layer 0% stenosis	4/16
Double layer 20% stenosis	16/16
Double layer 40% stenosis	15/16
Double layer 60% stenosis	15/16

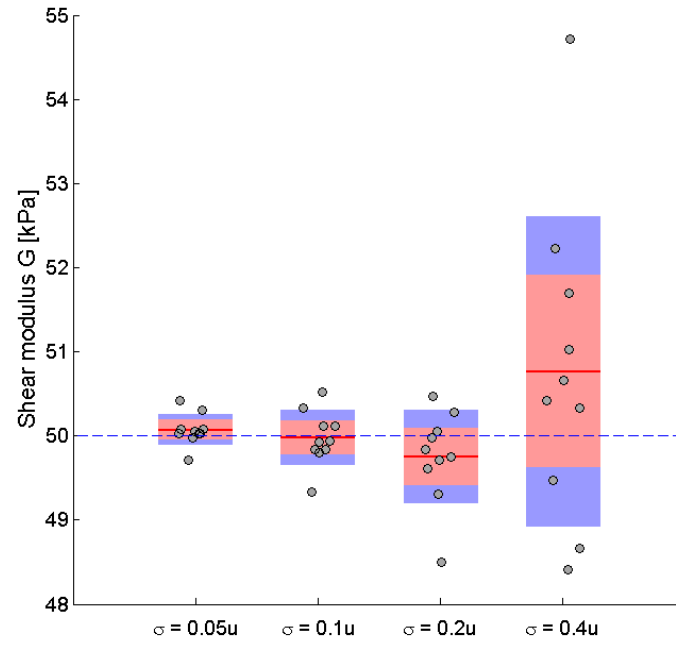


Figure 4.1: Results of the test case. Every dot is a shear modulus estimated by the inverse approach, based on a reference displacement field with noise.

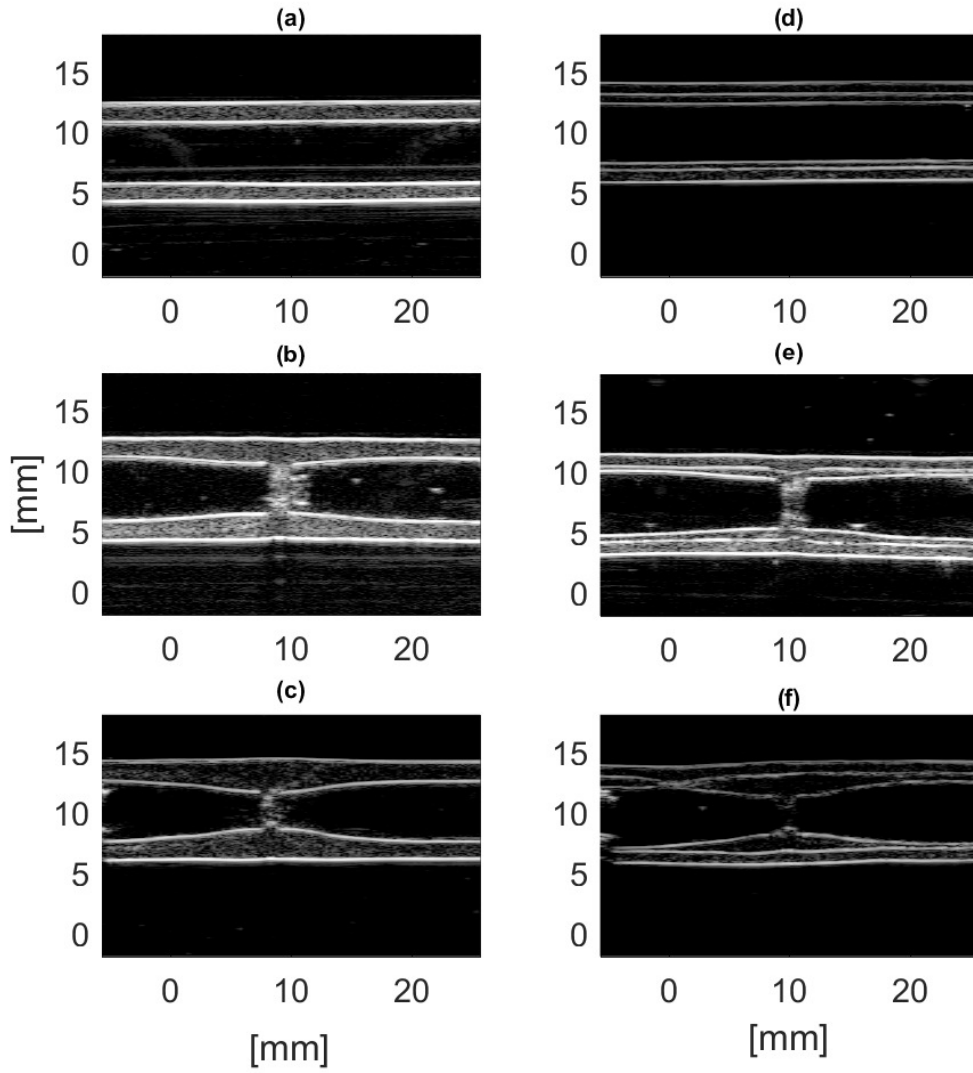


Figure 4.2: B-mode images of phantoms with different configurations. Increasing in complexity: single layer phantom without stenosis (a), single layer phantom with 20% stenosis (b), single layer phantom with 40% stenosis (c), double layer phantom without stenosis (d), double layer phantom with 20% stenosis (e), double layer phantom with 40% stenosis (f).

4.2 Phantom construction

PVA phantoms were used to test the inverse approach. The construction of phantoms with 60% stenosis were not successful. In the middle of the stenosis there was accumulation of PVA, which blocked the water flow. Therefore those phantoms had to be excluded. The other phantoms were successfully constructed without leakage: All single layer phantoms and the corresponding tensile test sheet are from the same batch of PVA. The 0% and 40% double layered phantoms and the corresponding tensile test sheets are from the same batch. The double layer phantom with 20% stenosis is re-imaged after a shelf time of 2 months. There was no corresponding tensile test sheet available. Figure 4.2 shows B-mode images of the constructed phantoms at $p = 0$ mmHg. In the stenosed phantoms, accumulated PVA is visible in the center of the phantom.

4.3 Displacement tracking

Figure 4.3 shows the displacement tracking for the single layered phantom with 40% stenosis. It is observed that the tracking points follow the phantom wall during inflation. However, around the stenosis at the luminal wall, some tracking points do not follow the luminal wall accurately. Similar patterns were observed for the other phantoms.

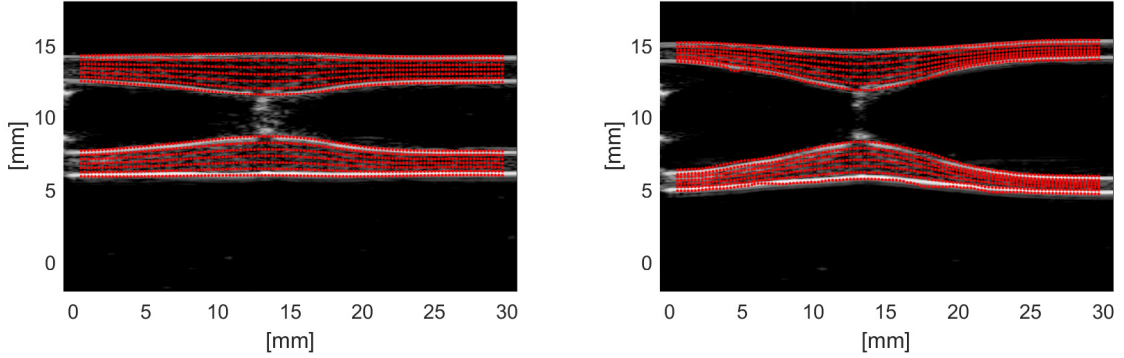


Figure 4.3: Displacement tracking in the single layered phantom with 40% stenosis. Left: $p = 0$ mmHg and right: $p = 80$ mmHg.

4.4 Estimation stress-free geometry

For every phantom the stress-free configuration was calculated with the backward displacement method. The maximal residual r_{max} for every iteration is displayed in Figure 4.4. r_{max} is defined according to equation 3.26. In the first iteration, the residual of every phantom is equal to the assigned displacement u_z , approximately 10 mm. After ± 16 iterations the maximum convergence is reached, with an error in the order of 10^{-5} mm. Only the double layer straight tube (D00) converges to $r_{max} = 10^{-4}$ mm.

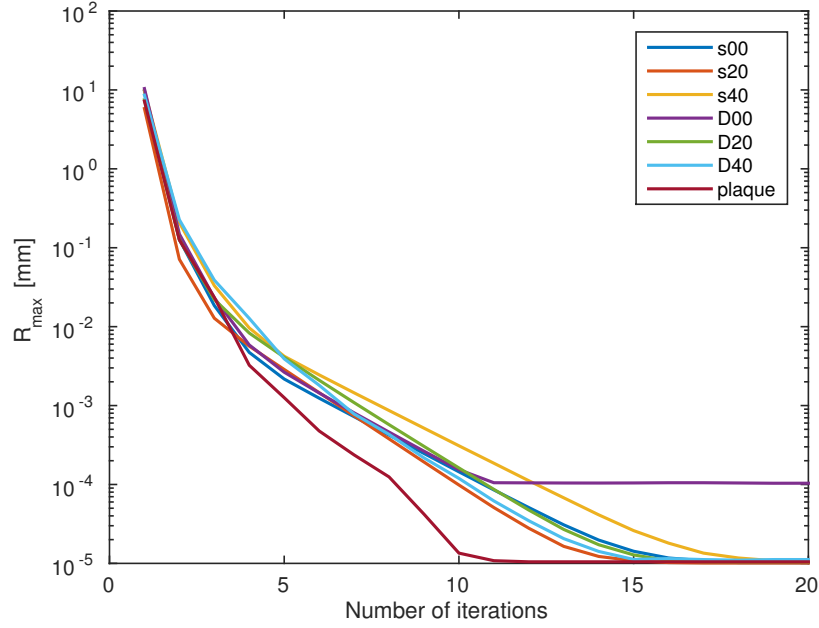


Figure 4.4: Convergence the backward displacement method for the different phantoms.

4.5 Material properties: Inverse Approach

4.5.1 Single layer phantoms

Table 4.2 shows the results of the inverse approach for single layer phantoms with different degrees of stenosis. Unfortunately, during the experiment a pressure drop over the phantom was measured. At the left side of the tube, the pressure range ranged 0 to 100 mmHg. On the right side the pressure range was approximately 0 to 60 mmHg. Therefore it was decided to redo the simulations with different pressure ranges: 0 to 100 mmHg and 0 to 80 mmHg. Hence, the estimated shear moduli are denoted by respectively $G_{FEM,100}$ and $G_{FEM,80}$. The magnitude of the average error is in the order $1 \cdot 10^{-1} \text{ mm}$. The estimated shear modulus decreases slightly for an increasing stenosis. In Figures 4.5, 4.7 and 4.9 the displacement fields U_{REF} and U_{FEM} are shown for the

Table 4.2: Results inverse approach: the single layer phantoms.

Tube geometry	λ_z	$G_{FEM,100}$	$G_{FEM,80}$	E
Single 0%	1.25	41.7 kPa	33.4 kPa	0.071 mm
Single 20%	1.14	39.1 kPa	31.3 kPa	0.137 mm
Single 40%	1.24	37.7 kPa	30.2 kPa	0.060 mm

different single layer phantoms. The absolute displacements on each node in a longitudinal cross section are displayed. U_{REF} is the displacements field obtained from the ultrasound image with displacement tracking. U_{FEM} is the displacements field of the finite element simulation which has the best match (minimum error E) with U_{REF} . The displacements in the simulated phantoms all show similar global patterns compared to the measured displacements. Figures 4.6, 4.8 and 4.10 show the differences between U_{REF} and U_{FEM} on each node in the longitudinal cross section. A few comments on the results:

- Figure 4.5 shows that the displacements in the upper wall are smaller compared to the lower wall, a difference of approximately 0.5 mm.

- In the stenosis the displacements around the outer wall are lower compared to the displacements in the rest of the tube (4.7 and 4.9).
- In 4.6, the simulated displacements deviate with a maximum of 0.2 mm, especially in the lower left wall.
- In 4.8 almost the complete simulated lower wall has lower displacements compared to the measured displacements. The simulated displacements in the upper wall are higher than the measured displacements. However in the stenosis, the displacements are lower.
- In the stenosis the simulated displacements are around 0.2 mm higher than the reference displacements (4.8 and 4.10).

4.5.2 Double layer phantoms

Table 4.3 shows the results of the inverse approach for double layer phantoms with different degrees of stenosis. The displacement tracking in the upper wall of the 20% stenosed phantom was not accurate due to air bubbles in the lumen. Therefore, only the displacements in the lower wall were used as reference displacements. To see the effect of the different reference displacement fields, the inverse approach was applied twice to the double layered phantom with 40% stenosis. Once, with both, the lower and upper wall as reference displacement field and again, with only the lower wall as reference displacement field. The maximum differences is 8% in $G_{inn,80}$ and 5% in $G_{out,80}$. As expected from the *in silico* testing, the optimization algorithm was not able to estimate the material properties of the double layer straight phantom. For the double layer phantoms with stenosis the estimated shear modulus of the outer layer is around 41 kPa. For the shear modulus of the inner layer there was a difference between the 20% and 40% stenosed phantom of 34%.

Table 4.3: Results inverse approach: the double layer phantoms.

Tube geometry	λ_z	$G_{inn,80}$	$G_{out,80}$	E
Double 0%	1.27	-	-	-
Double 20% lower wall	1.20	27.9 kPa	41.1 kPa	0.047 mm
Double 40%	1.27	20.2 kPa	40.1 kPa	0.119 mm
Double 40% lower wall	1.27	18.7 kPa	41.8 kPa	0.111 mm

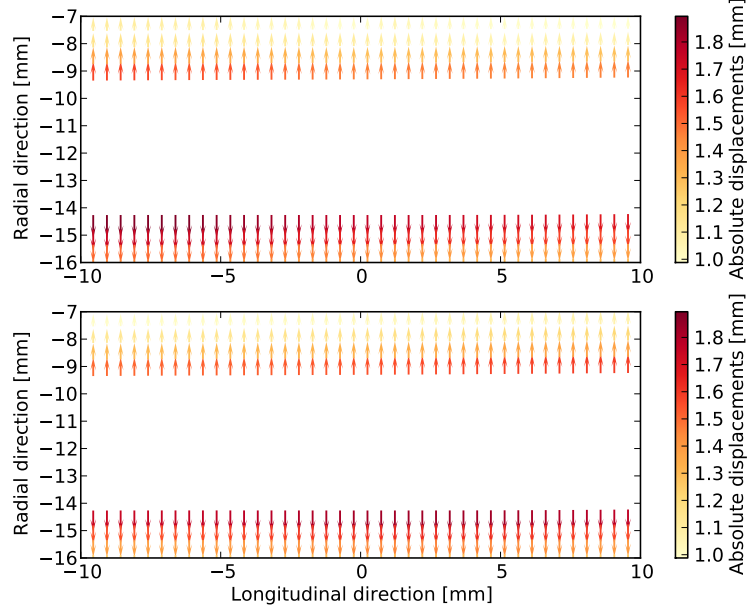


Figure 4.5: The displacement fields U_{REF} and U_{FEM} for the single layer phantom without stenosis.

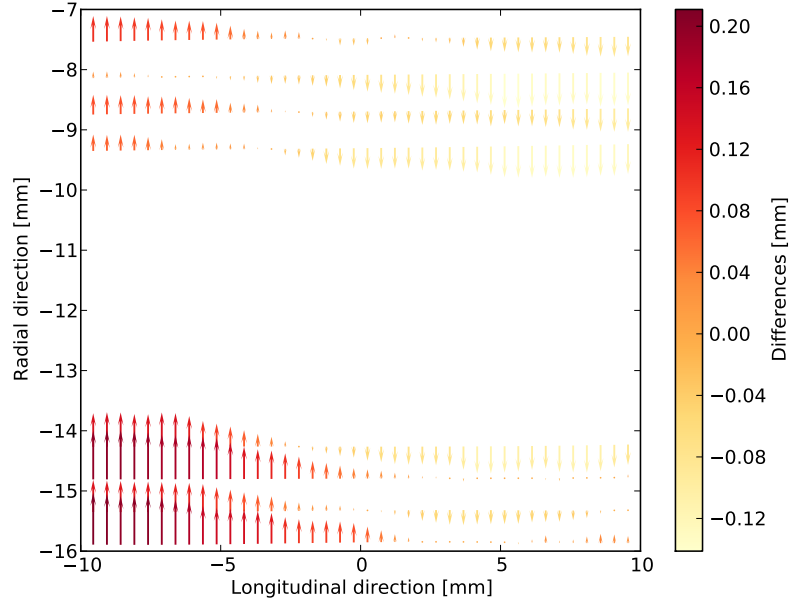


Figure 4.6: The displacement field differences on each node ($U_{REF} - U_{FEM}$) for the single layer phantom without stenosis after applying the inverse approach.

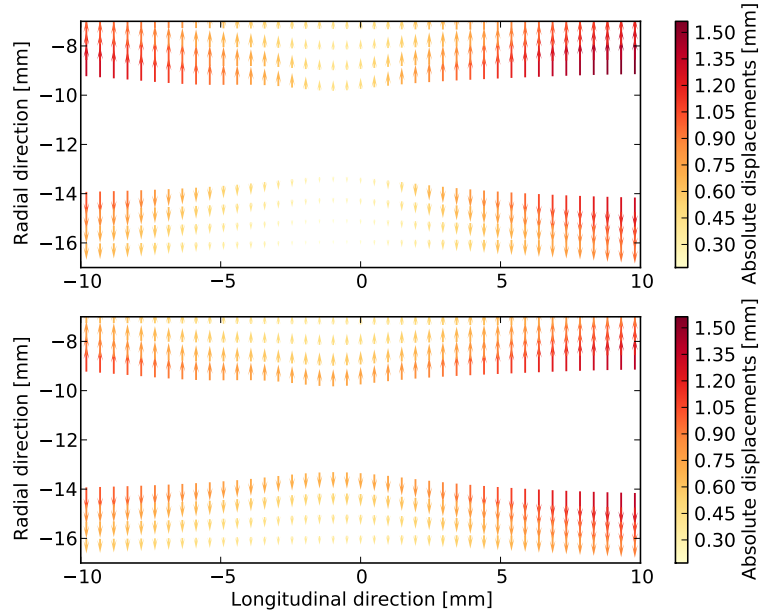


Figure 4.7: The displacement fields U_{REF} and U_{FEM} for the single layer phantom with 20% stenosis.

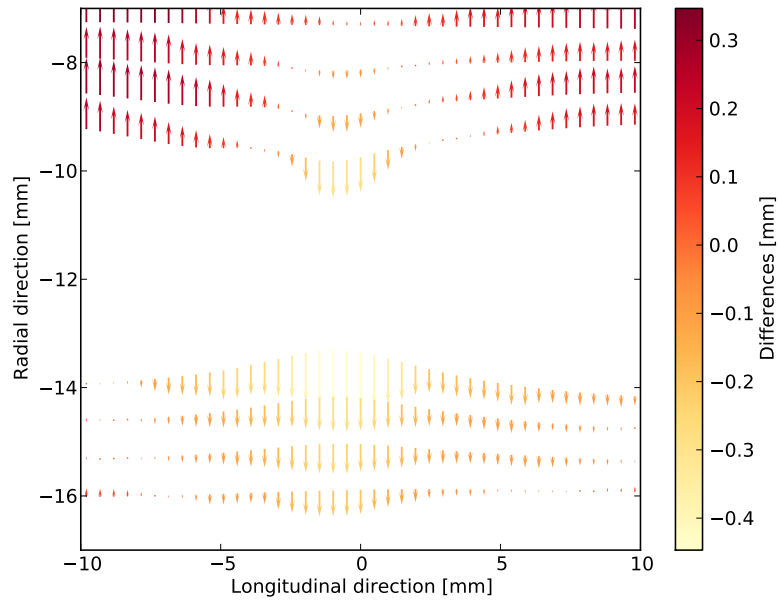


Figure 4.8: The displacement field differences on each node ($U_{REF} - U_{FEM}$) for the single layer phantom with 20% stenosis after applying the inverse approach.

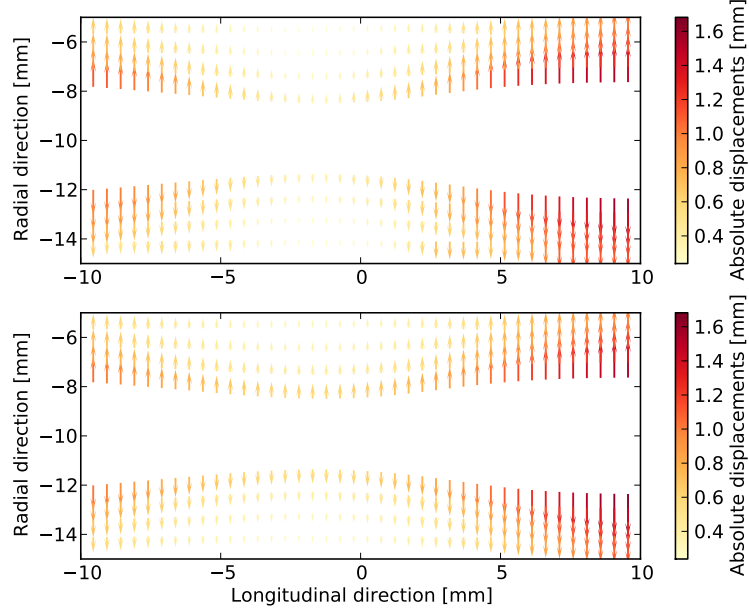


Figure 4.9: The displacement fields U_{REF} and U_{FEM} for the single layer phantom with 40% stenosis.

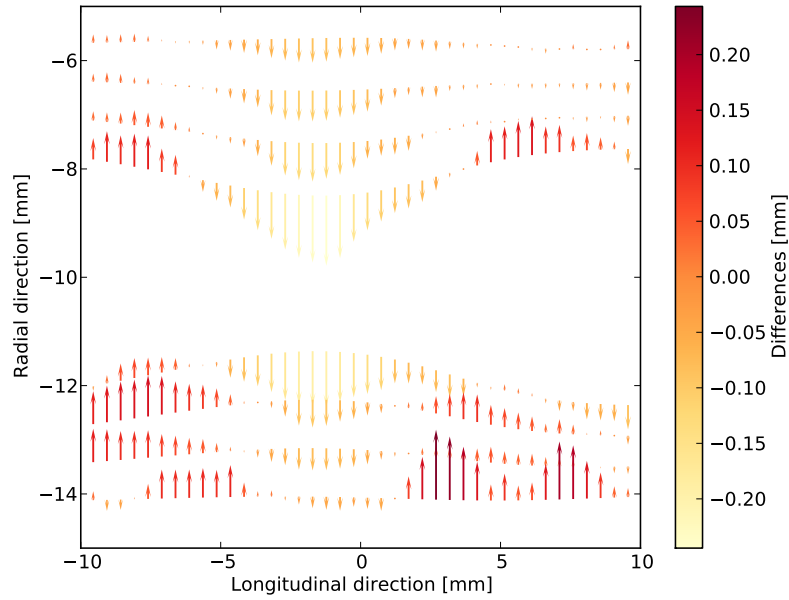


Figure 4.10: The displacement field differences on each node ($U_{REF} - U_{FEM}$) for the single layer phantom with 40% stenosis after applying the inverse approach.

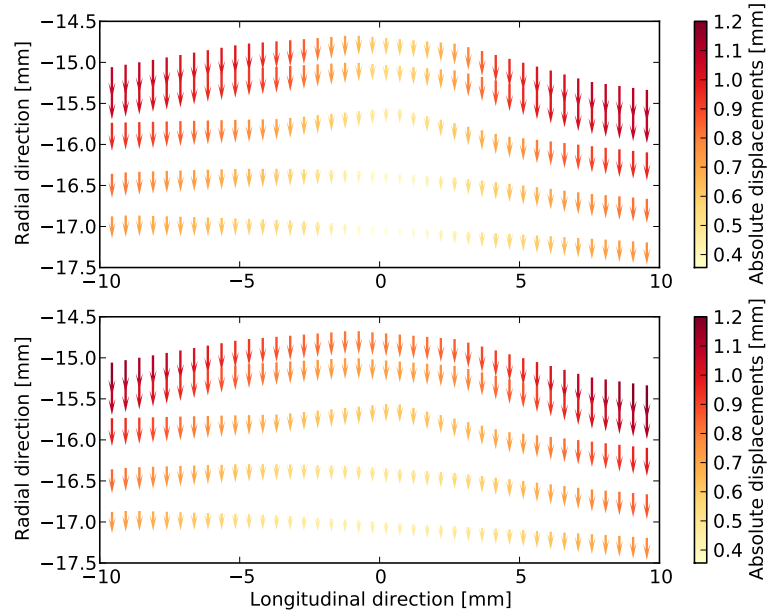


Figure 4.11: The displacement fields U_{REF} and U_{FEM} for the double layer phantom with 20% stenosis.

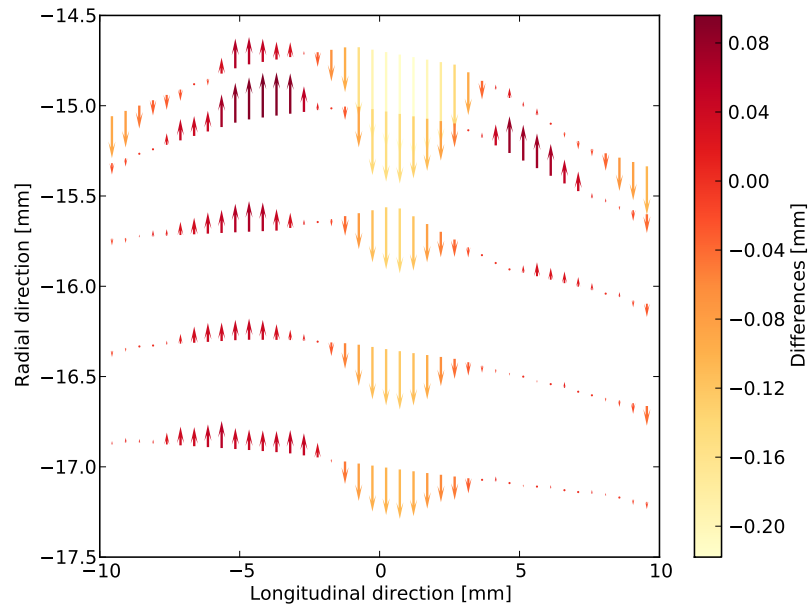


Figure 4.12: The displacement field differences on each node ($U_{REF} - U_{FEM}$) for the double layer phantom with 20% stenosis after applying the inverse approach.

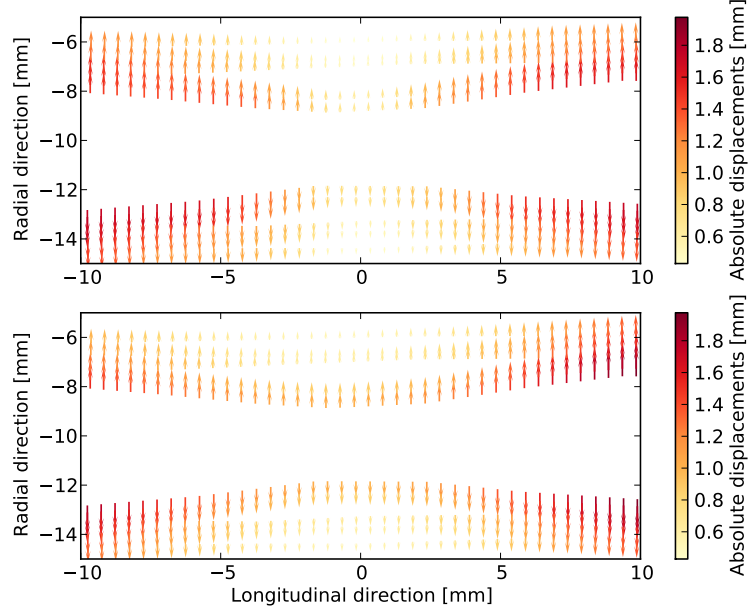


Figure 4.13: The displacement fields U_{REF} and U_{FEM} for the double layer phantom with 40% stenosis.

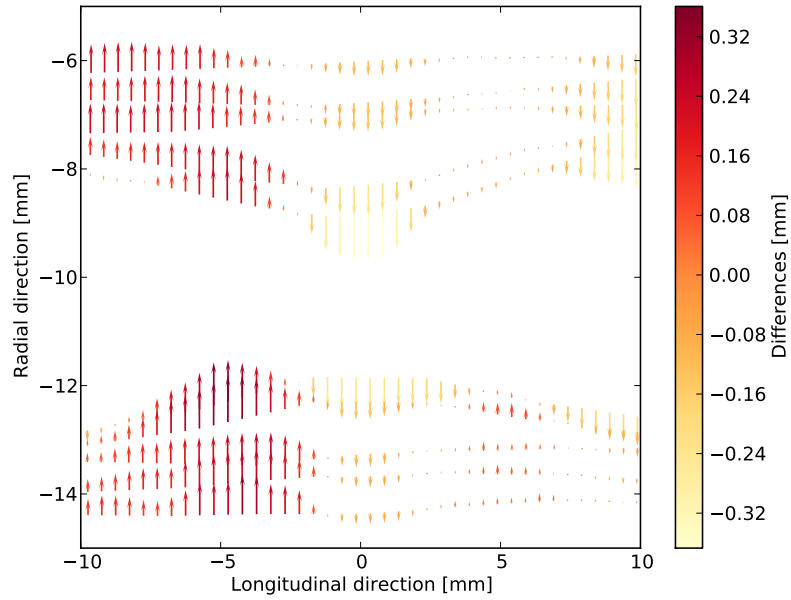


Figure 4.14: The displacement field differences on each node ($U_{REF} - U_{FEM}$) for the double layer phantom with 40% stenosis after applying the inverse approach.

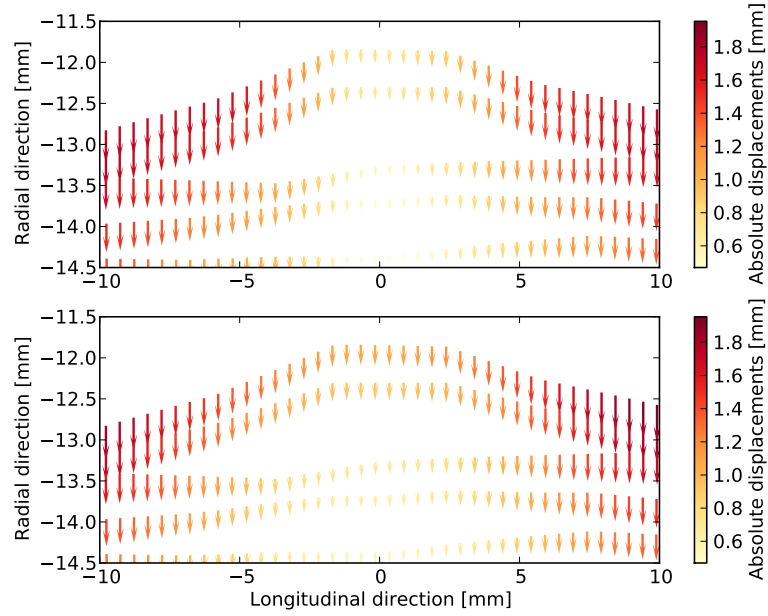


Figure 4.15: The displacement fields U_{REF} and U_{FEM} of the lower wall of the double layer phantom with 40% stenosis.

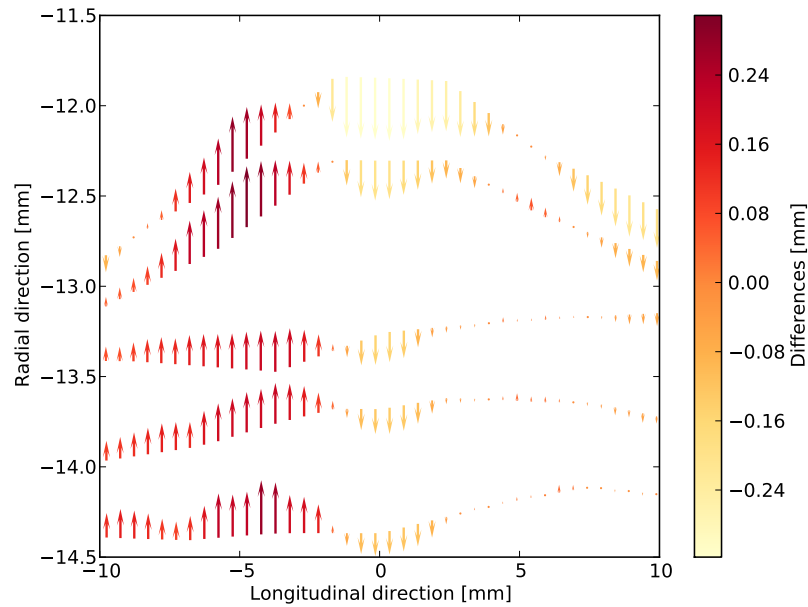


Figure 4.16: The displacement field differences on each node of the lower wall ($U_{REF} - U_{FEM}$) for the double layer phantom with 40% stenosis after applying the inverse approach.

4.6 Material properties: Uni-axial Tensile Test

Figure 4.17 shows two typical stress- finger strain curves from the uni-axial test. It shows clearly that PVA with 2 f/t cycles is less stiff than PVA that was exposed to 4 f/t cycles. In table 4.4 the finger strain of each phantom is used to calculate a shear modulus of the tensile tests. From every PVA sheet 4-5 samples are measured. There was no PVA sheet available corresponding to the double layer phantom with 20% stenosis.

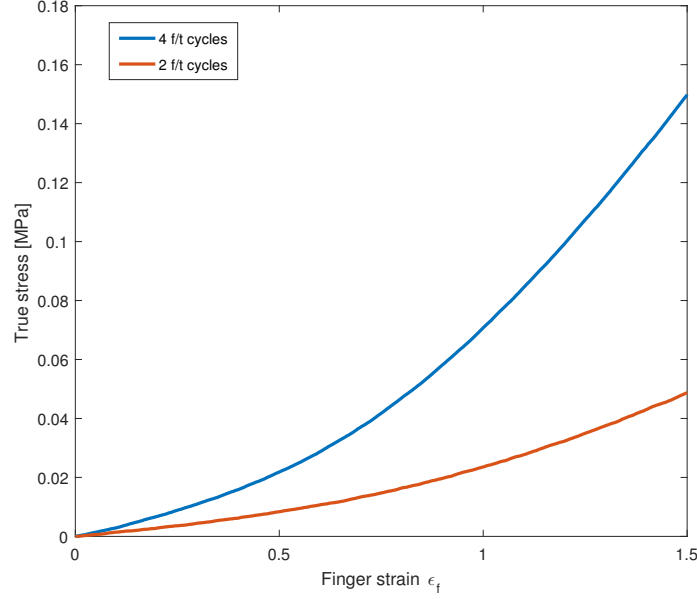


Figure 4.17: Stress- finger strain curves from the uni-axial tensile test. Blue line for a sample exposed to 4 freeze/thaw cycles, the red line for a sample exposed to 2 freeze/thaw cycles.

Table 4.4: Results of the uni-axial tensile test. The range used to determine G_{TT} is based on the finger strain $\epsilon_{\theta\theta}$ of the corresponding phantom. Two different measures of the diameter are used: the diameter to the middle of the wall (d_m) and the diameter based on the inner wall (d_i).

Tube Diameter	Range (G_{TT}) Middle (d_m)	mean(G_{TT}) Middle (d_m)	Range (G_{TT}) Inner (d_i)	mean(G_{TT}) Inner (d_i)
Single 0%	26.1 - 30.5 kPa	27.8 kPa	34.0 - 39.4 kPa	35.8 kPa
Single 20%	22.6 - 26.5 kPa	24.0 kPa	27.9 - 32.5 kPa	29.5 kPa
Single 40%	21.8 - 25.5 kPa	23.2 kPa	27.6 - 32.1 kPa	29.1 kPa
Double 0% outer	26.0 - 31.7 kPa	29.0 kPa	36.1 - 43.0 kPa	39.8 kPa
Double 0% inner	-	-	9.0 - 13.0 kPa	11.0 kPa
Double 20%	-	-	-	-
Double 40% outer	23.7 - 29.0 kPa	26.4 kPa	36.2 - 43.1 kPa	39.9 kPa
Double 40% inner	-	-	9.0 - 13.0 kPa	11.0 kPa

4.7 Tensile test versus inverse approach

Figure 4.18 gives an overview of the results of the inverse approach compared with the tensile tests. Here, G_{TT} was based on the finger strain ($\epsilon_{f,\theta}$) of the luminal wall. G_{FEM} is the estimated shear modulus estimated with the inverse approach, based on a pressure range from 0 to 80 mmHg. The results of the double layer phantom with a 20% stenosis are not displayed, since there is no corresponding tensile test data.

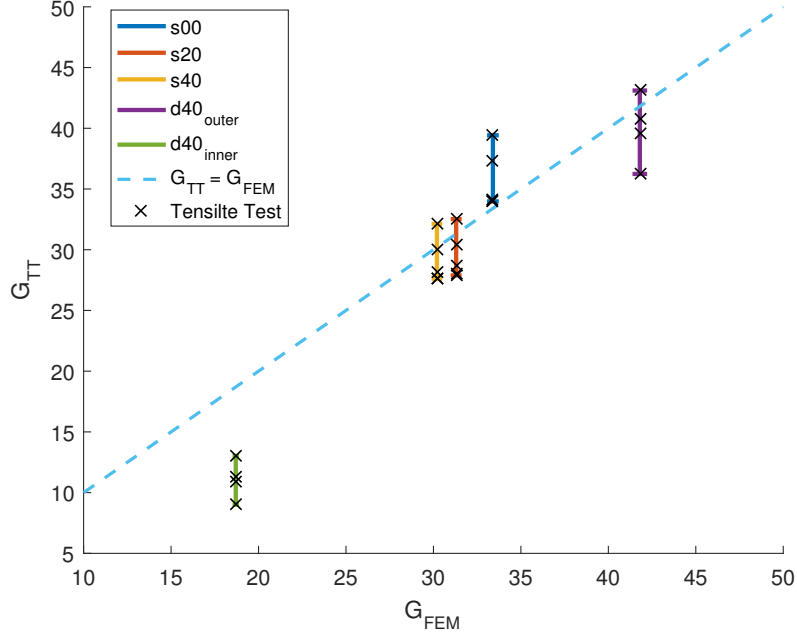


Figure 4.18: The material properties estimated with the inverse approach G_{FEM} vs. the material properties of the tensile test G_{TT} , based on the maximum stretch range of the tube.

Chapter 5

Discussion

In this study an inverse approach was developed and used to determine material properties of artificial carotid phantoms. The method was validated using uni-axial tensile testing. There is always a trade-off between mimicking the *in vivo* situation as accurately as possible versus creating a straight-forward experimental set-up. The latter results in a clear validation of the inverse approach. In this study, the former option was chosen, to work towards an *in vivo* application of the inverse approach.

5.1 Phantom construction and inflation experiment

The construction of the phantoms was not always successful. The mold that creates the lumen consists of two parts, which can be attached to each other. During the construction of the phantoms, PVA flows in between the two parts. This results in extra PVA in the middle of the stenosis, see figure 5.1. This extra material is not taken into account in the simulation, but the material will influence the reference displacements U_{REF} . This can lead to an over estimation of the material properties. In case of the double layer phantoms this will result in a higher value for G_{inner} . During the inflation experiment is the phantom pressurized from 0 to 100 mmHg by

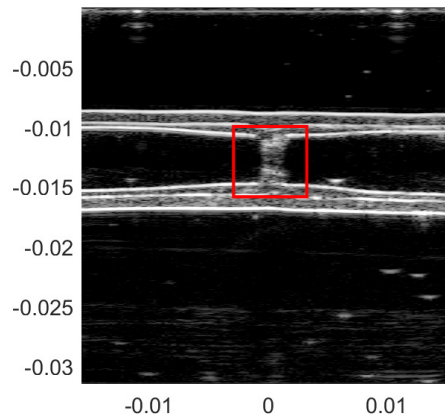


Figure 5.1: Double layered phantom with 20% stenosis, the extra PVA in the middle of the stenosis is marked with the red square.

pumping water through the phantom. This pressure is measured prior to the phantom. However, when the pressure is measured on the other side, the pressure is approximately 0 to 60 mmHg. In the simulations, it is assumed that the water flow can be neglected and only the hydrostatic

component needs to be taken into account, see equation 3.4. The pressure drop as well as this assumption result in a high uncertainty of the pressure modelled in the tube. This uncertainty will have a significant influence on the results, see table 4.2. The displacement tracking was performed successfully, see Figure 4.3. However, due to noise in the lumen, the tracking points were moved towards the lumen during inflation. So the displacements at the luminal wall were underestimated, this occurred especially in phantoms with a stenosis.

5.2 Geometry construction

A mesh/geometry is constructed from the ultrasound image of the phantom. It is observed that the dimensions of the constructed geometry do not always match the dimensions of the molds. The measured wall thickness of the upper and lower wall were not always equal, based on the molds an axisymmetric geometry is expected. The phantom was imaged and after a 180 degree rotation the imaging was repeated. It was observed that the measured differences are caused by the construction of the phantom. Besides irregularities in the construction of the phantom, the probe position may have an influence. Figure 5.2 shows a simulation which displays the dimensions of the tube versus the probe position relative to the center line of the tube. If the probe is slightly shifted from the center line, the wall thickness will be overestimated and the diameter will be underestimated. Due to the 2-D geometry construction, it is important that probe is exactly positioned above the center line of the phantom.

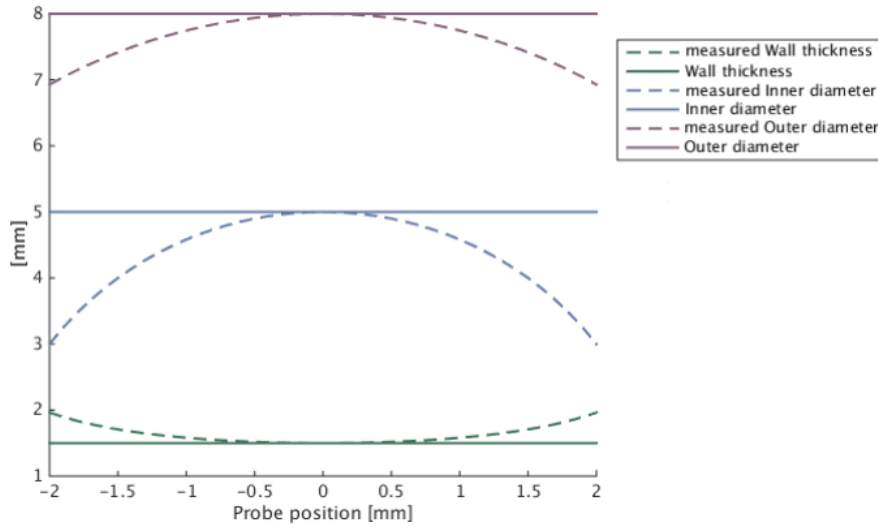


Figure 5.2: Simulation of the influence of the probe position relative to the phantom on the measured wall thickness, inner diameter and outer diameter.

5.3 Inverse approach: Method

In the inflation experiment, the stress due to the longitudinal pre-stretch (σ_L) is unknown. *In vivo* the situation is more complex. Here, the zero-pressure configuration is also unknown, since the artery is imaged at diastolic pressure. To estimate the stress tensor σ_L , the stress-free configuration \mathbf{X}_0 is required. The configuration \mathbf{X}_0 could be determined by the geometry of the mold or by imaging the stress-free configuration. Both options were tested, however the geometry calculated by applying the pre-stretch to the estimated geometry \mathbf{X}_0 , was not similar to the measured geometry \mathbf{X}_L . Possible explanations are:

- The PVA phantom can expand by absorbing water, so \mathbf{X}_0 is not equal to the geometry of the mold.
- The longitudinal pre-stretch was not measured accurately.
- The material model does not describe the material behavior correctly.
- Errors in constructing the measured configuration \mathbf{X}_L obtained from ultrasound imaging and manual segmentation.

To overcome this problem the backward displacement method was used to estimate the stress-free configuration. This method was performed with an initial guess for the material properties, this is possible since an incompressible material model is used. So the obtained stress-free configuration was independent of the chosen shear modulus G used in the backward displacement method. An advantage of using this method is that it can be applied *in vivo* as well. By assuming for instance a pre-stretch based on statistical data (for example related to age as described by Horný et al. [20]), the stress-free configuration can be estimated. An other (practical) advantage is that the matching between the tracking points and the mesh is straight-forward.

A 2-D displacement field is used as reference to match with the displacements of finite element simulations. On each wall there were approximately 5-6 tracking points obtained in radial direction and 30 tracking points in longitudinal direction. The tracking points at both ends of the tube were excluded from this reference field for mainly two reasons. First, to reduce the influence of the boundary conditions at both ends. In the inflation experiment a thin rope and a plastic extension piece were used to attach the phantom to the experimental set-up. The second reason is that the US image did not cover the complete phantom, so the mesh was extended on both sides. However, the exact size of extension on both sides was not always clear. The radial displacements are dependent on the length of the chosen extension, especially in simulations of stenosed phantoms. Therefore the displacements on both ends were not taken into account. It was tested to use only displacements of lower wall of the double layer phantom with 40% stenosis as reference displacements. Table 4.3 shows the results of the parameter estimation, the difference are quite small: $\pm 8\%$ difference for the inner wall and $\pm 5\%$ for the outer wall.

To model the material behavior of PVA, a neo-Hookean material model was chosen. The model only consists of one material property, which reduces the number of material parameters that need to be estimated, but limits the description of non-linear material behavior. The stress-strain curve in figure 4.17 shows clearly that PVA does not behave like a neo-Hookean solid. A straight curve is expected from an neo-Hookean material, see equation 3.42. However, when a small strain or stress range is studied, this range could be approximated by a neo-Hookean curve. The same applies to the *in vivo* situation for a carotid artery. The vascular wall does not behave like a neo-Hookean solid [19]. However, at the small pressure range in an human artery, approximately 80 to 120 mmHg, it can be approximated with this material model. In the inflation experiment a larger pressure range was used, so using this material model is not the best choice. We could have used a non-linear model, but for the *in vivo* application this is unnecessary. Moreover, increasing model complexity introduces uncertainties in the parameter estimates. Hence, in future work, the inflation tests should be redone for a physiological pressure range. Fromageau et al. [12] has shown that the Poisson ratio of PVA is between 0.42 and 0.48, depending on the number of freeze/thaw cycles. So PVA is close to incompressible.

In the inverse approach, an inflation experiment is simulated. It is assumed that the phantom consists of a material with an equally distributed stiffness for each layer. The stiffness of PVA depends on the freeze-thaw process. During freezing, the temperature gradient is in the radial direction, from the stainless steel tube to the Perplex mold. So it is likely that there is a gradient in stiffness in the radial direction of the phantom, the magnitude of this effect is unknown. When a double layered phantom is constructed, the inner layer is poured into the mold after two f/t cycles. The influence of this process on the stiffness of the outer layer is unknown. The boundary between the inner and outer layer is modelled as a sharp boundary in terms of stiffness. In reality there will be a smooth distribution of stiffness in the radial direction over the boundary.

5.4 Inverse approach: Results

The test case showed that the optimization algorithm was able to find the global minimum, independent of the initial guess. However, in the case of straight double layered tubes the optimization algorithm was not able to find a global minimum in 12 out of 16 start positions. Irregularities in the geometry, such as a stenosis, create a global minimum for a double layered tube. This was expected and also reflected in the results of the inverse approach applied to phantoms: in the double layered straight tube the algorithm was not able to find a minimum.

The second test case showed that Gaussian noise on the reference displacements has little effect on the shear modulus estimation. Even with high noise ($\sigma = 0.4 \cdot U_{REF}^i$) the estimated shear moduli derogates less than 5% from the actual shear modulus. The reason for this is that the average noise is equal to zero ($\mu = 0$). The applied Gaussian noise does influence the error E , but does not shift the location of the minimum. The actual type of noise due to ultrasound imaging and displacement tracking is yet unknown, so it is hard to predict its influence. This test case shows that the magnitude of the error E , does not always relate to the success of the parameter estimation.

The backward displacement method was successfully used to determine the initial geometry for every phantom, in approximately 15 iterations. This means that solving problem \mathcal{S}_L (equation 3.6) resulted in the measured geometry \mathbf{X}_L . Of course, the calculated stress tensor $\boldsymbol{\sigma}_L$ is still an estimation, depending on the material properties chosen.

Overall, the simulated displacement fields and measured displacements have similar patterns. The average displacement in each node of the single layer straight tube was 1.4 mm. The average error on each node is reduced to values between 0.047-0.137 mm. So the average error is between 3% and 10% of the average displacements. In phantoms with a stenosis, the simulated displacements in the stenosis are often higher than in the displacements measured. A possible explanation is the accumulation of PVA in the stenosis, which is not taken into account in the simulation. The estimated shear moduli of the single layer phantoms are more similar. This is expected since the PVA material is from the same batch and practically the same pressure was applied. In the double layer phantom with 20% stenosis, the estimated shear modulus for the inner layer is 25% higher than the phantom with 40% stenosis. The 20% stenosed phantom was imaged after 2 months cooling in the refrigerator, this could have an effect on the material properties. An other explanation could be the accumulated PVA in the 20% stenosed phantom.

5.5 Uni-axial Tensile test

To validate the inverse approach uni-axial tensile tests were performed. The PVA specimen were constructed from the same batch of PVA-gel and were frozen simultaneously with the phantoms. All the molds were constructed from stainless steel and Plexiglas, this should result in a similar freeze-thaw process. The tensile test samples were cut in different direction. An uni-axial tensile test is compared with an inflation experiment. In the latter the material is stretched in two directions, first a pre-stretch in longitudinal direction and subsequently pressurized, which results in a circumferential stretch. This is compared with a PVA sample that is stretched in only one direction. This does not result in a straightforward comparison. Bi-axial tensile testing could be used to stretch the sample in two directions, similar to the inflation experiment. Uni-axial tensile testing was chosen because the measurements are more accurate.

5.6 Tensile tests versus inverse approach

The finger strain in circumferential direction of the inflation experiment was matched to the finger strain in the tensile direction. In this comparison, a higher circumferential finger strain ($\epsilon_{f,\theta}$) results in a higher matching shear modulus G_{TT} . In contrast to the inverse approach, where larger displacements, and thus a higher circumferential finger strain, will result in a lower estimate of the shear modulus G_{FEM} (with similar pressure). This contradictory relation, renders

the validation study to be prone to errors. Figure 4.18 shows an overview of the validation of the inverse approach. The estimated shear moduli G_{FEM} of the single layer phantoms are within the range of G_{TT} . $\epsilon_{f,\theta}$ decreased for an increasing degree of stenosis. This makes sense since the stenosis prevents movements of the wall. The shear modulus of the outer layer of the 40% stenosed phantom is in agreement with the tensile test. The shear modulus found for the inner wall, is lower than expected from the tensile test. In figure 4.18, the values of G_{TT} were based on the finger strain $\epsilon_{f,\theta}$ of the lumen wall. If G_{TT} was based on the middle diameter, the estimated values for G_{FEM} would be higher than G_{TT} (see table 4.4)

5.7 Future work

- To describe the stress/strain relation of PVA more accurately, a different material model could be used. The number of material parameters that need to be estimated, should be reduced to a minimum, preferable one for each material. In the case of more than one material parameter for each material, the function to be minimized (similar to equation 3.28), will probably have multiple local minima and higher uncertainties. A possible solution is to assign constant values to certain material parameters, values based on experiments or literature, that are not identifiable *in vivo*, so it is still possible to estimate values for the other material parameters.
- The inverse method could be tested with an *in vivo* pressure range, 80 mmHg to 120 mmHg. This was not possible on the experimental data of this research, due to the irregularities in the pressure signal. When the *in vivo* pressure range is used, an extra step is needed to determine the configuration and wall stress of the phantom at zero pressure. This could be performed with the backward incremental method by De Putter et al. [10].
- In this research the phantom with a fatty plaque made by R. Boekhoven was analysed, but the optimization algorithm was not able to find a global minimum. The geometry was based on a 2-D US image of this phantom and prior information on the construction of the phantom. However, the geometry is not axi-symmetric. A geometry construction based on multiple 2-D images under different angles would improve the geometry construction. This would also result in more reference displacements, so there is more information available to estimate the three different material properties. The construction of the fatty plaque phantom should be repeated, since there are no tensile-test specimen available for the validation. The long shelf-time may have changed the material properties.
- The validation in this research was not straight-forward. The main limitations were the uncertainties of the pressure in the phantom, and the comparison between an uni-axial test and an inflation experiment. To solve the latter limitation, bi-axial tensile testing could be performed, similar to Lopata et al. [26]. Instead of pressurizing the phantom with circulating water, the phantom could be simply pressurized with water by blocking the water flow at one end of the tube. This would result in a more accurate estimation of the pressure inside the phantom. This way of pressurizing the phantom is more similar to the applied pressure in the finite element simulation.
- The flexibility of the PVA phantom construction could be used to create different types of phantoms. It would be interesting to create phantoms with a different stiffness in longitudinal directions. For example, apply four f/t cycles to the right side of the phantom and only two f/t cycles to the left side of the phantom. Will the inverse approach be able to find the differences in stiffness between the left and right side of the phantom?
- The final steps would be to apply the inverse approach to *in vivo* data. Healthy carotid arteries and finally diseased carotid arteries with a fatty plaque could be imaged *in vivo* and validated *in vitro*. This would give additional challenges compared to using experimental data: The US image quality will be reduced, due to surrounding tissue, calcifications

and motion of the patient and the US probe during the image acquisition. Since arteries of patients are not axi-symmetric, the artery should be imaged with respect to multiple different angles. To construct a 3-D mesh, the different 2-D images should be combined. Due to presence of tissue surrounding the artery, segmentation of the vascular wall will be less straight-forward. The luminal pressure in the artery is unknown and more difficult to estimate. Brachial pressure is most likely the only measurement.

- There are several modelling challenges *in vivo*: the carotid artery is not imaged at zero pressure, so the zero pressure configuration and stress are unknown. The pre-stretch is unknown, and should be based on experimental data. The material behavior of the vascular wall is more complex compared to PVA. For small pressure range, the material behavior could be approximated with the neo-Hookean material model. However, the vascular wall will be more heterogeneous and the morphology is unknown. The different materials can not be distinguished with ultrasound. The artery is surrounded by different tissues, so the outer wall of the artery is subjected to different boundary conditions.

5.8 Conclusion

An inverse approach was developed and tested on carotid phantoms. With this method we were able to estimate global material properties of single layered phantoms with different degree of stenosis. With this method we were also able to distinguish between a weaker inner layer and a stiffer outer layer for stenosed PVA phantoms, however the absolute values of the estimated shear modulus, especially for the inner layer, of these phantoms still showed a bias. In future work, this methodology will be extended to possibly identify the presence of lipid in the arterial wall, and monitor the development of plaques over time.

Chapter 6

Appendix

Protocol PVA Preparation

Materials

1. Polyvinyl alcohol (PVA) (Mowiol, 28-99, Sigma Aldrich) with Mw 145,000, 99.0-99.8 mol % hydrolysis.
2. Ultrasound scatterers (Orgasol 2001, Arkema France), which have an average size of 5.8 μ m.
3. Scale and heating plate with temperature controller
4. Plastic cup with blue lid and glass beaker (a little bigger than the plastic cup)
5. Magnetic stir bean
6. Spatula to stir
7. Soft plastic stopper or small lid (to place on the bottom of the glass beaker, so the plastic cup doesn't get in contact with the glass)
8. Glass stopper (or something else that is a little heavy but small, that you can place on top of the lid of the plastic cup when it's in the water so the cup stays put)

Preparation (a solution of 15wt% (1 wt% scatterers))

1. Place the scale and the heating plate with temperature controller in the fumehood
2. Place the soft plastic stopper in the glass beaker. Fill it with water, be sure it doesn't spill when you place the plastic cup in the water so the top of the lid is at the same height as the edges of the beaker (test this!)
3. Put the glass beaker with water on the plate. Hang the thermometer of the temperature controller in the water. Set the temperature of the heating plate at 85°C. Set it at high heating speed.
4. Put the stir bean in the plastic cup and place the plastic cup and the lid next to it on the scale (write down the weight). Set scale to zero.
5. First weigh 1 g of scatterers (only take out the plastic bag that contains the scatterers in the fume hood!) put them directly in the plastic cup.
6. Add PVA to a total of 15 g.
7. Carefully add demi H₂O to a total of 100 g and stir the mixture with the spatula. Close the lid tightly.

8. When the water is at 85C, carefully place the plastic cup with the PVA solution in the water. Place the glass stopper on top. Turn on the magnetic stir function of the heating plate.
9. Leave to dissolve for 4 hours. Check the solution every 15 minutes and stir with the spatula.
10. After 4 hours take the plastic cup out of the water and leave it at room temperature for 4 hours.
11. Use the PVA gel directly (for best results) or store at 4C. It stays useable for about 2 weeks. Before using, bring it to room temperature.

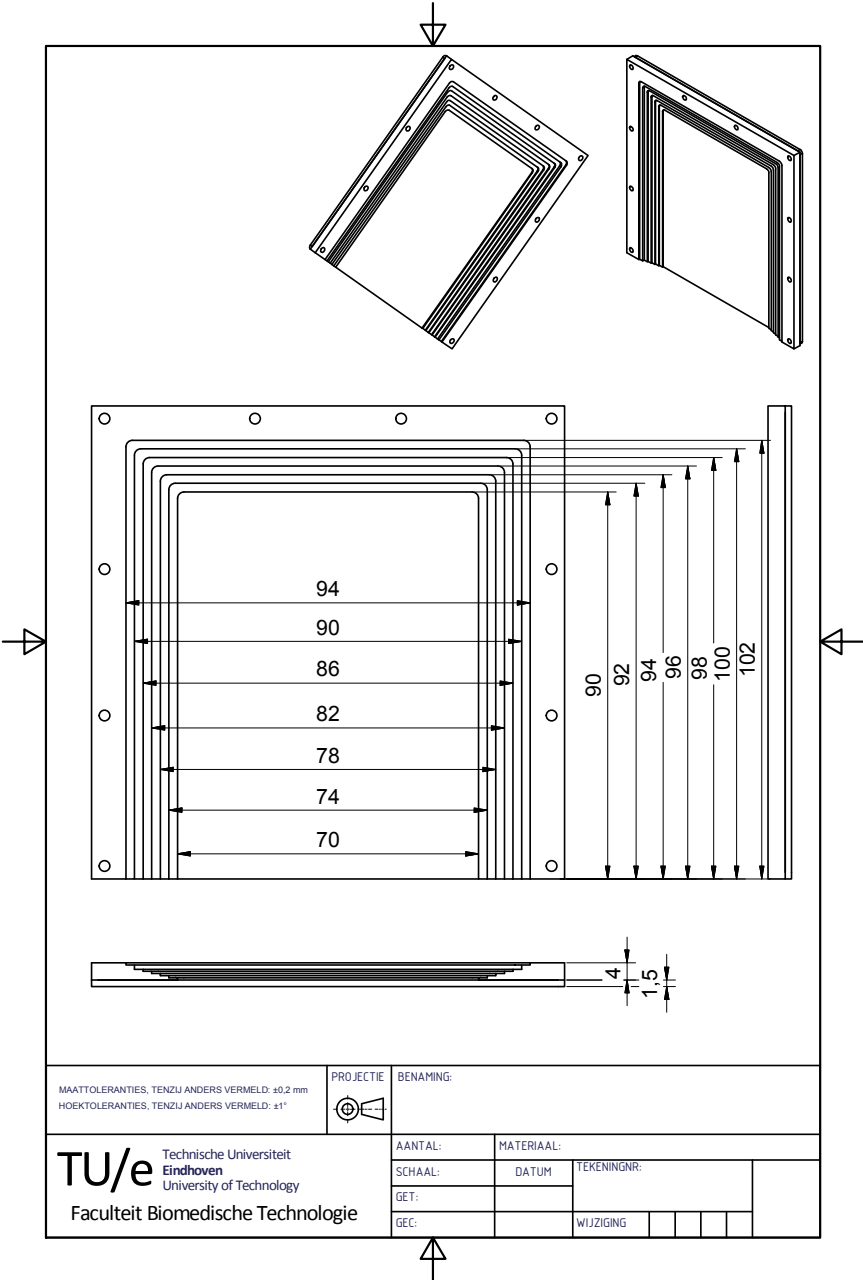


Figure 6.1: Composition of the square mold.

Bibliography

- [1] Radj A Baldewsing, Frits Mastik, Johannes A Schaar, Patrick W Serruys, and Antonius FW van der Steen. Youngs modulus reconstruction of vulnerable atherosclerotic plaque components using deformable curves. *Ultrasound in medicine & biology*, 32(2):201–210, 2006. 8
- [2] Radjkumarsing A Baldewsing, Mikhail G Danilouchkine, Frits Mastik, Johannes A Schaar, Patrick W Serruys, and Antonius FW van der Steen. An inverse method for imaging the local elasticity of atherosclerotic coronary plaques. *IEEE Transactions on Information Technology in Biomedicine*, 12(3):277–289, 2008. 8
- [3] A Benetos, S Laurent, AP Hoeks, PH Boutouyrie, and ME Safar. Arterial alterations with aging and high blood pressure. a noninvasive study of carotid and femoral arteries. *Arteriosclerosis, Thrombosis, and Vascular Biology*, 13(1):90–97, 1993. 7
- [4] RW Boekhoven, Richard GP Lopata, and Frans N Van De Vosse. Mechanical characterisation of healthy and diseased carotid arteries using ultrasound. 2015. 7, 8, 17, 19
- [5] Joris Bols, Joris Degroote, Bram Trachet, Benedict Verhegghe, Patrick Segers, and Jan Vierendeels. A computational method to assess the in vivo stresses and unloaded configuration of patient-specific blood vessels. *Journal of computational and Applied mathematics*, 246:10–17, 2013. 10, 11, 12
- [6] Seemant Chaturvedi, Askiel Bruno, T Feasby, R Holloway, O Benavente, SN Cohen, R Cote, D Hess, J Saver, JD Spence, et al. Carotid endarterectomyan evidence-based review report of the therapeutics and technology assessment subcommittee of the american academy of neurology. *Neurology*, 65(6):794–801, 2005. 6
- [7] Hao Chen, Hairong Shi, and Tomy Varghese. Improvement of elastographic displacement estimation using a two-step cross-correlation method. *Ultrasound in medicine & biology*, 33(1):48–56, 2007. 19
- [8] Chris L De Korte, Gerard Pasterkamp, Anton FW Van Der Steen, Hein A Woutman, and Nicolaas Bom. Characterization of plaque components with intravascular ultrasound elastography in human femoral and coronary arteries in vitro. *Circulation*, 102(6):617–623, 2000. 7
- [9] CL De Korte, EI Cespedes, AFW Van der Steen, B Norder, and K Te Nijenhuis. Elastic and acoustic properties of vessel mimicking material for elasticity imaging. *Ultrasonic imaging*, 19(2):112–126, 1997. 8
- [10] S De Putter, BJBW Wolters, MCM Rutten, M Breeuwer, FA Gerritsen, and FN Van de Vosse. Patient-specific initial wall stress in abdominal aortic aneurysms with a backward incremental method. *Journal of biomechanics*, 40(5):1081–1090, 2007. 44
- [11] MM Dooley, PM Meaney, and JC Bamber. Evaluation of an iterative reconstruction method for quantitative elastography. *Physics in medicine and biology*, 45(6):1521, 2000. 8

- [12] Jérémie Fromageau, Elisabeth Brusseau, Didier Vray, Gérard Gimenez, and Philippe Delachartre. Characterization of pva cryogel for intravascular ultrasound elasticity imaging. *IEEE transactions on ultrasonics, ferroelectrics, and frequency control*, 50(10):1318–1324, 2003. 42
- [13] YC Fung and SQ Liu. Change of residual strains in arteries due to hypertrophy caused by aortic constriction. *Circulation Research*, 65(5):1340–1349, 1989. 9
- [14] Spyretta Golemati, Antonio Sassano, M John Lever, Anil A Bharath, Surinder Dhanjil, and Andrew N Nicolaides. Carotid artery wall motion estimated from b-mode ultrasound using region tracking and block matching. *Ultrasound in medicine & biology*, 29(3):387–399, 2003. 7
- [15] Hendrik HG Hansen, Richard GP Lopata, and Chris L de Korte. Noninvasive carotid strain imaging using angular compounding at large beam steered angles: validation in vessel phantoms. *IEEE transactions on medical imaging*, 28(6):872–880, 2009. 7
- [16] HHG Hansen, RGP Lopata, T Idzenga, and CL De Korte. Full 2d displacement vector and strain tensor estimation for superficial tissue using beam-steered ultrasound imaging. *Physics in Medicine and biology*, 55(11):3201, 2010. 8
- [17] J Hardamar. Lectures on cauchy problems, 1952. 8
- [18] APG Hoeks, PJ Brands, FAM Smeets, and RS Reneman. Assessment of the distensibility of superficial arteries. *Ultrasound in medicine & biology*, 16(2):121–128, 1990. 8
- [19] Gerhard A Holzapfel, T Christian Gasser, and M Stadler. A structural model for the viscoelastic behavior of arterial walls: continuum formulation and finite element analysis. *European Journal of Mechanics-A/Solids*, 21(3):441–463, 2002. 8, 42
- [20] Lukáš Horný, Tomáš Adámek, and Markéta Kulvajtová. A comparison of age-related changes in axial prestretch in human carotid arteries and in human abdominal aorta. *Biomechanics and modeling in mechanobiology*, pages 1–9, 2016. 42
- [21] Jay D Humphrey. *Cardiovascular solid mechanics: cells, tissues, and organs*. Springer Science & Business Media, 2013. 25
- [22] Jaan Kiusalaas. *Numerical methods in engineering with Python 3*. Cambridge university press, 2013. 13, 14
- [23] Stephane Laurent, Bernard Caviezel, Lionel Beck, Xavier Girerd, Eliane Billaud, Pierre Boutouyrie, Arnold Hoeks, and Michel Safar. Carotid artery distensibility and distending pressure in hypertensive humans. *Hypertension*, 23(6 Pt 2):878–883, 1994. 7
- [24] Simon Le Floc’h, Jacques Ohayon, Philippe Tracqui, Gérard Finet, Ahmed M Gharib, Roch L Maurice, Guy Cloutier, and Roderic I Pettigrew. Vulnerable atherosclerotic plaque elasticity reconstruction based on a segmentation-driven optimization procedure using strain measurements: theoretical framework. *IEEE transactions on medical imaging*, 28(7):1126–1137, 2009. 8
- [25] Richard GP Lopata, Hendrik HG Hansen, Maartje M Nillesen, Johan M Thijssen, and Chris L De Korte. Comparison of one-dimensional and two-dimensional least-squares strain estimators for phased array displacement data. *Ultrasonic imaging*, 31(1):1–16, 2009. 19
- [26] Richard GP Lopata, Mathijs FJ Peters, Jan Nijs, Cees WJ Oomens, Marcel CM Rutten, and Frans N van de Vosse. Vascular elastography: a validation study. *Ultrasound in medicine & biology*, 40(8):1882–1895, 2014. 23, 24, 44

- [27] Shanthi Mendis, Pekka Puska, Bo Norrving, et al. *Global atlas on cardiovascular disease prevention and control*. World Health Organization, 2011. 6
- [28] John A Nelder and Roger Mead. A simplex method for function minimization. *The computer journal*, 7(4):308–313, 1965. 13
- [29] J Ophir, I Cespedes, Hm Ponnekanti, Y Yazdi, and Xin Li. Elastography: a quantitative method for imaging the elasticity of biological tissues. *Ultrasonic imaging*, 13(2):111–134, 1991. 7
- [30] Hermine Ribbers, Richard GP Lopata, Suzanne Holewijn, Gerard Pasterkamp, Jan D Blankensteijn, and Chris L De Korte. Noninvasive two-dimensional strain imaging of arteries: validation in phantoms and preliminary experience in carotid arteries in vivo. *Ultrasound in medicine & biology*, 33(4):530–540, 2007. 7
- [31] Michael S Richards and Marvin M Doyley. Non-rigid image registration based strain estimator for intravascular ultrasound elastography. *Ultrasound in medicine & biology*, 39(3):515–533, 2013. 8
- [32] MS Richards and MM Doyley. Investigating the impact of spatial priors on the performance of model-based ivus elastography. *Physics in medicine and biology*, 56(22):7223, 2011. 8
- [33] Peter M Rothwell and Charles P Warlow. Prediction of benefit from carotid endarterectomy in individual patients: a risk-modelling study. *The Lancet*, 353(9170):2105–2110, 1999. 6
- [34] Linda K Ryan and F Stuart Foster. Tissue equivalent vessel phantoms for intravascular ultrasound. *Ultrasound in medicine & biology*, 23(2):261–273, 1997. 8
- [35] Johannes A Schaar, Chris L de Korte, Frits Mastik, Chaylendra Strijder, Gerard Pasterkamp, Eric Boersma, Patrick W Serruys, and Anton FW van der Steen. Characterizing vulnerable plaque features with intravascular elastography. *Circulation*, 108(21):2636–2641, 2003. 7
- [36] Cédric Schmitt, Gilles Soulez, Roch L Maurice, Marie-France Giroux, and Guy Cloutier. Noninvasive vascular elastography: toward a complementary characterization tool of atherosclerosis in carotid arteries. *Ultrasound in medicine & biology*, 33(12):1841–1858, 2007. 7
- [37] Hang Si. Tetgen, a delaunay-based quality tetrahedral mesh generator. *ACM Transactions on Mathematical Software (TOMS)*, 41(2):11, 2015. 21
- [38] Chantal N Van den Broek, Arjen Van der Horst, Marcel CM Rutten, and Frans N Van De Vosse. A generic constitutive model for the passive porcine coronary artery. *Biomechanics and modeling in mechanobiology*, 10(2):249–258, 2011. 18
- [39] David Vancraeynest, Agnes Pasquet, Véronique Roelants, Bernhard L Gerber, and Jean-Louis J Vanoverschelde. Imaging the vulnerable plaque. *Journal of the American College of Cardiology*, 57(20):1961–1979, 2011. 7